# Multimodal identification of rare potent effector CD8 T cells in solid tumors

Arja Ray[1,2], Molly Bassette[1,2], Kenneth H. Hu[1,2,#], Lomax F. Pass[1,2], Bushra Samad[2,3], Alexis Combes[1,2,3,5], Vrinda Johri[2,3], Brittany Davidson[2,3], Grace Hernandez[4], Itzia Zaleta-Linares[1,2], Matthew F. Krummel[1,2*]

**Affiliations:**
[1]Department of Pathology, [2]ImmunoX Initiative, [3]UCSF CoLabs, [4]Department of Anatomy, [5]Department of Medicine, University of California, San Francisco, CA 94143, USA. [#] Current Address: Department of Immunology, The University of Texas MD Anderson Cancer Center and James P Allison Institute

***Corresponding Author:**
Matthew F. Krummel, Ph.D.
513 Parnassus Avenue, HSW 512
San Francisco, CA 94143-0511
matthew.krummel@ucsf.edu
Tel: (415) 514-3130
Fax: (415) 514-3165

**Abstract:** Antitumor immunity is driven by CD8 T cells, yet we lack signatures for the exceptional effectors in tumors, amongst the vast majority of CD8 T cells undergoing exhaustion. By leveraging the measurement of a canonical T cell activation protein (CD69) together with its RNA (*Cd69*), we found a larger classifier for TCR stimulation-driven effector states *in vitro* and *in vivo*. This revealed exceptional 'star' effectors—highly functional cells distinguished amidst progenitor and terminally exhausted cells. Although rare in growing mouse and human tumors, they are prominent in mice during T cell-mediated tumor clearance, where they engage with tumor antigen and are superior in tumor cell killing. Employing multimodal CITE-Seq allowed de novo identification of similar rare effectors amidst T cell populations in human cancer. The identification of rare and exceptional immune states provides rational avenues for enhancement of antitumor immunity.

**One sentence summary:** Parsing T cell activation states using a novel reporter mouse reveals the functional identity of potent anti-tumor CD8 T cells

38 **Main Text:**

39 Within broadly immunosuppressive tumor microenvironments (TME), pockets of rare reactive
40 immunity have been discovered, such as those containing conventional type 1 dendritic cells
41 (cDC1s) that support T cells through antigen presentation (*1*). T cells, which integrate their
42 encounters with antigens over their lifetime (*2-4*), require potent antigen stimulation for anti-tumor
43 function. Yet chronic stimulation by persistent antigen in the TME also drives precursor TCF7$^{hi}$
44 CD8 T cells to dysfunctional or exhausted states (*5*) and cells with phenotypes defined as resident
45 memory ($T_{RM}$) also show strong evidence of exhaustion(*6*). Although this path to T cell exhaustion
46 is increasingly well understood including developmental stages (*7, 8*), molecular markers (*9-11*),
47 transcriptional, epigenetic (*10-13*) and microenvironmental drivers (*14, 15*) , an intermediate and
48 reactive T cell effector population that emerges from these precursors is not well-defined.

49 ***A novel genetic tool to report T cell stimulation history in vivo*:** While the cell surface
50 expression of a protein like CD69 is often linked to successful T cell stimulation and T cell retention
51 (*16*), our analysis of a series of datasets showed that a history of repeated stimulation is
52 associated with decreasing transcription of the *Cd69* gene. For example, *Cd69* mRNA itself is
53 higher in naïve vs. effector and progenitor vs. terminally exhausted CD8 T cells **(Fig. S1A-C)**, and
54 in conventional T cells in tumor-adjacent normal areas versus those within paired human
55 colorectal cancers (CRC) (**Fig. S1D**). Further mining of related data reveals that the transcription
56 factors regulating *Cd69* transcription were also differentially and systematically lower in exhausted
57 vs. naïve CD8 T cells (**Fig. S1E**). In contrast, CD69 protein expression, driven by TCR stimulation
58 or other stimuli such as interferons (*17*), is often uncoupled from transcriptional activity at this
59 locus by strong 3' UTR-mediated post-transcriptional regulation (*18*). We thus reasoned that
60 tracking *Cd69* RNA alongside its protein may together provide a useful means to differentiate the
61 historical and current effector state of T cells.

62 To make this tractable, we generated mice in which DNA encoding the teal fluorescent protein
63 (TFP) was inserted at the 5' end of the *Cd69* locus to record its transcriptional activity (hereby
64 referred to as the *Cd69*-TFP reporter) **(Fig. 1A)**. In concert with antibody staining for surface CD69
65 protein, we thus had a non-invasive way to study, sort and challenge cells with different
66 combinations of RNA and protein expression. In unchallenged *Cd69*-TFP mice, the majority
67 (~80% "Q1", **Fig. 1B**) of CD8 T cells in lymph nodes were $TFP^{hi}$ without expressing surface CD69.
68 Another small population of cells expressed CD69 protein on their cell surface alongside TFP
69 (~5%, "Q2") and a moderate population (~15% "Q3") was low for both TFP and CD69 (**Fig. 1B**).
70 We validated that TFP accurately reflected *Cd69* RNA expression at steady state (**Fig. S2A-B**)
71 and found that the reporter faithfully tracked with well-established CD69 protein upregulation
72 during the early and intermediate stages of thymic positive selection (*19*) as well as during the
73 first 6-18h of stimulation of isolated peripheral T cells with anti-CD3/CD28 beads (**Fig. S3A, B**).

74 When viewed across differentiation states, we found that TFP expression varied with extent and
75 quality of historical stimulation; $CD44^{hi}CD62L^{lo}$ Effector CD8 T cells expressed levels lower than
76 $CD44^{lo}CD62L^{hi}$ Naïve cells as we had observed in historical datasets and $CD44^{lo}CD62L^{hi}$ central
77 memory T cells (Memory) demonstrated higher levels than either. (**Fig. 1C).** These differences in
78 TFP expression were stable when cells were purified and rested in IL-7 overnight (**Fig. 1D**).
79 Predictably, following short (3h) stimulation with anti-CD3/anti-CD28 beads, $TFP^{hi}$ Memory and
80 $TFP^{lo}$ Effectors (**Fig. S4A**) both rapidly upregulated surface CD69, even when new transcription
81 was blocked by Actinomycin D, but maintained their pre-existing TFP status (**Fig. 1E**). However,
82 *de novo* surface CD69 expression was markedly lower in $TFP^{lo}$ cells upon stimulation as
83 compared to $TFP^{hi}$ (**Fig. 1E-F, Fig. S4B**), consistent with dependency of protein expression on
84 the level of transcript. Together this indicated faithful reporter activity and also that a combination
85 of *Cd69* RNA reporting (TFP) and CD69 protein exposed a difference (i.e. Q2 vs. Q4) between
86 recently activated cells with different histories of antigen experience.

87 To directly study how *Cd69*-driven TFP levels were related to activation history, we set up
88 repetitive "chronic" stimulation cultures using purified CD8 T cells from *Cd69*-TFP mice. Cells
89 were subjected to 3 cycles of 48h stimulation with 1:1 anti-CD3/anti-CD28 beads, followed by 72h
90 rest under either hypoxia (1.5% $O_2$ to mimic the TME) or normoxia, in the presence of low
91 concentrations of IL-2 after the first cycle (**Fig. 1G, Fig. S5A**). CD69 protein expression rose after
92 each stimulation, although significantly less so by the 3rd stimulation, while expression of the
93 activation marker CD44 became more pronounced (**Fig 1G, Fig. S5A**). *Cd69*-driven TFP levels
94 also rose following each stimulation, but progressively rested each time to lower levels, an effect
95 that culminated in about a 50% and 30% reduction under hypoxia and normoxia after 3 cycles,
96 respectively (**Fig 1G-H, Fig. S5A, B**). We validated that both native *Cd69* mRNA (**Fig. 1J, Fig.
97 S5C**) as well as the upstream transcription factor *Jun* (**Fig. 1K**), decreased over the cycles, albeit
98 with faster initial decay than TFP, perhaps reflecting a longer half-life of the fluorescent protein as
99 compared to the transcript that it reports. Repeated stimulation concurrently upregulated
100 exhaustion markers such as PD1, CD38 and Tim-3(*20*) (**Fig. 1L, Fig. S5D, E**). Provision of IL-2
101 in absence of additional anti-CD3/anti-CD28 stimulation (**Fig. S5F**) demonstrated that
102 differentiation (**Fig. S5G**), decline in TFP expression (**Fig S5H**), and acquisition of exhaustion
103 markers (**Fig. S5I**) were not simply a function of time. While declining levels of resting mRNA did
104 not prevent re-expression of TFP and CD69 upon stimulation, it significantly lowered the
105 magnitude of the peaks from Cycle 1 to Cycle 3 (**Fig. 1M, Fig. S5J**), consistent with previous data
106 (**Fig. S4B**). Thus in the Protein:RNA (CD69:TFP) space, trajectories of cell state are not retraced
107 during subsequent activation events—rather, TFP levels decrease with repeated stimulation (**Fig.
108 1N**)."Q2" cells in this reporter system emerge as ones that are recently activated, yet have not
109 been subject to chronic and exhaustive stimulation.

110

111 **Delineation of chronic vs. potent activation states in tumors:** To translate these observations
112 into the context of tumors, we adoptively transferred *Cd69*-TFP reporter positive ovalbumin-
113 reactive CD8 T cells from CD45.1; OT-I; mice into WT mice bearing B78chOVA (OVA and
114 mCherry expressed in B78 (*14*)) tumors (**Fig. 2A**). Recovered cells were largely in Q1 and Q3 on
115 when they can be first detected at day 4, and by day 6, we found them predominantly in the "Q2"
116 (~60%) $TFP^{hi}CD69^{+}$ state. By day 14, however, they were primarily $TFP^{lo}CD69^{-}$ (Q3) and
117 $TFP^{lo}CD69^{+}$ (Q4) (**Fig. 2B, D).** In contrast, the distribution of adopted cells was more consistent
118 in the draining lymph node (dLN) across time: approximately 60% in Q1 and 15-30% in Q2. (**Fig.
119 2C, D**). Similar trends were observed in a spontaneous breast carcinoma tumor model
120 (PyMTchOVA)(*21*) (**Fig. S6A, B**).

121 Even at day 14, Q2 cells expressed less terminal exhaustion markers as compared to those in
122 the $TFP^{lo}$ Q4 in both B78chOVA (**Fig. 2E)** and PyMTchOVA tumors **(Fig. S6C**) and Q4 cells
123 largely became prevalent in tumors approximately 10 days post-adoption (**Fig. 2B-D, Fig. S6A,
124 B**). The decline in the Q2 proportion of OT-Is from d6 to d18 was also accompanied by a decrease
125 in progenitor (Ly108) and increase in terminal exhaustion markers (**Fig. S6D**).

126 Because ongoing recruitment of T cells from the dLN is difficult to control and may obscure
127 interpretation of these adoptive transfer experiments, we complemented these results by
128 developing a variant of a long-term tumor slice overlay protocol(*22*) where all T cells encounter
129 the tumor microenvironment at once and no new emigrants arrive (**Fig. 2F**). The progression of
130 phenotypes through CD69:TFP quadrants (**Fig. 2G, Fig. S7A)** and the increasing over-
131 representation of cells with an exhausted phenotype in Q4 (**Fig. S7B-D**) recapitulated what we
132 had seen in vivo, suggesting that this is not a result of variations in the lymph-node emigrating
133 pool. Slices also allowed easy analysis of robust proliferation in the slice-infiltrating OT-I T cells
134 over time using violet proliferation dye (VPD) (**Fig. S7E**) which accompanied the general decrease
135 in TFP expression with each division (**Fig. S7F**) and was exemplified at day 3 **(Fig. S7G**). VPD

136 dilution showed that Q4 cells had typically undergone more division (**Fig. S7H**) as they acquired
137 higher levels of exhaustion (**Fig. 2H**) as compared to Q2 cells, further differentiating these states.
138 This progression is consistent with previous studies of the relationship between chronic tumor
139 residence, proliferation(*23, 24*) and exhaustion, while also again differentiating the population in
140 Q2.

141 Finally, to determine how this progression is related to antigen detection and the
142 microenvironment in which that antigen is detected, we isolated CD8 T cells with a non-tumoral
143 specificity (LCMV-specific P14; *Cd69*TFP) and compared their state both within a tumor (that
144 does not express their antigen) and within a vaccination site, to that of the OT-Is (**Fig 2I**). P14;
145 *Cd69*TFP cells co-injected with CD45.1; OT-I; *Cd69*TFP T cells into B78chOVA tumor-bearing
146 mice, that also received a priming gp33-41 peptide vaccination distal to the tumor (**Fig. 2I**), were
147 found to express higher TFP levels in the tumor than OT-Is (**Fig. 2J, K**). In contrast to the Q4-
148 rich OT-I T cells in the tumor, P14 T cells at the contralateral vaccination site remained
149 substantially $TFP^{hi}$ with a 4x increase in the frequency of cells Q2 (**Fig. 2J, K**). Hence, exposure
150 to the TME alone did not lead to loss of a Q2 state, and presentation of antigen at a vaccine site
151 stimulated cells in such a way as to maintain that Q2 state.

152

153 **Marking the highest-quality intratumoral effectors:** We next sought to both understand
154 whether Q2 cells were typically better effectors and use transcriptomic analysis to find signatures
155 that tracked best with Q2 cells. We thus isolated OTI; *Cd69* TFP T cells from d12 B78chOVA
156 tumors, sorted and barcoded each population separately for CD69:TFP quadrant and performed
157 single cell RNA Sequencing (scSeq) (**Fig. 3A**). Analysis of this data via Louvain clustering and
158 UMAP projection allowed us to immediately map Q2 in the context of previously defined post-
159 exhaustion T cell states ($T_{EX}$) (*8*), and other previously named intratumoral states that were based
160 on RNA alone (**Fig. 3B, Fig. S8A**). Our data recapitulated those computationally derived predicted

161 differentiation trajectories (**Fig. S8B, C**; See Methods) and the expected progression towards
162 terminal exhaustion through the quadrants Q1-Q4 (**Fig. S9**)). Unbiased computational RNA-
163 based clustering alone, however, did not capture a single subset with a superior cytotoxic score
164 (*Prf1, Klrd1, Gzmc, Tnfrsf9, Ifng*), which was variably distributed across multiple subsets, although
165 these are indeed more frequent within with exceptional levels in populations that have previously
166 been named $Tex^{E.Eff}$ , $Tex^{int}$ and especially $Tex^{KLREff}$ (**Fig 3C**).

167 When we overlayed barcodes representing Q2 sorted cells onto this UMAP, we found that these
168 spanned several clusters, and as expected with dominance in those $Tex^{Eff}$ ($Tex^{E.Eff}$, $Tex^{KLREff}$)
169 populations as well as a subregion of the $Tex^{Prog}$ (**Fig. 3D, Fig. S10A, B**). Further and consistent
170 with our previous observations, parsing these effectors by *Cd69*:TFP quadrant demonstrated the
171 Q2 subset to be low and Q4 to be highest in a signature (*Pdcd1, Cd38, Cd39, Entpd1, Tox*) of
172 exhaustion (**Fig. 3E**). Using this, we sought to use Q2 as an anchor, to characterize the
173 transcriptional signature of the strongest effectors with robust cytotoxicity and limited exhaustion.
174 We did so first by illuminating the intersection of $Tex^{Eff}$ and Q2, identifying a population that
175 perhaps due to its sparsity and subtlety, doesn't otherwise appear as a distinct computational
176 cluster. Performing DGE analysis of Q2 vs. Q4 within that $T_{EX}^{Eff}$, we found a signature comprising
177 among others the granzyme *Gzmc,* a tetraspannin previously implicated in lymphocyte activation
178 (*25, 26*) *Cd81* and a collection of other genes that are consistent with a unique propensity to
179 interact with other cells such as *Xcl1 (*putatively would attract cDC1*)* and *Ccr7.* Perhaps
180 unsurprisingly for a population that may have unique stimulatory signals, we also found
181 enrichment election of a subset of proliferation-associated genes.(**Fig. 3F**).

182 The resulting signature, which we term 'star' effectors or $T^*_{EFF}$ for simplicity, highlights a portion
183 of $Tex^{Prog}$ as well as a subset of cells buried within $Tex^{E.Eff}$ and $Tex^{KLR\ Eff}$ on a uMAP projection.
184 (**Fig 3G**). These overlap only partially with cells that express the highest levels of *Tcf7* and are
185 nearly exclusive from those that are highest in markers of exhaustion (**Fig. 3G, Fig. S11A**). The

186 distribution of this signature also tracks with genes associated with cytotoxicity (e.g. *Ifng*, which
187 notably is not part of the signature), and significantly with *Cd81,* which in contrast is a component
188 of the signature(**Fig. 3G**). Cd81 is a surface protein, making it useful for sorting but turns out to
189 vary in its fidelity for reporting star effector phenotypes across various TME. For example, in the
190 B78chOVA tumors, Q2 was reliably associated with ~3x increases in the mean level of CD81
191 surface protein expression (**Fig. 3H**), where in other models such as PyMTchOVA showed that
192 this marker can also be found in cells that have not upregulated CD69 protein **(**i.e. Q1, **Fig. S11C)**.
193 Such variability limits absolute use of CD81 as a definitive marker across every tumor and site,
194 and the use of this single marker in the PyMT model may be further limited since $CD81^+$ $T^*_{EFF}$s
195 were even rarer within these tumors (**Fig. S11B, D**).

196 Nonetheless, in the B78 tumor model, armed with a refined definition of $T^*_{EFF}$ that could be non-
197 invasively assessed through the combination of the Q2 reporter marking together with CD81
198 antibody staining, we sought to assess how effector function parsed with this population. For this
199 we sorted OT-I T cells by the CD69:TFP quadrants with CD81 stain from tumors at d12 and
200 assayed for cytokine and granzyme expression following restimulation with PMA/Ionomycin for
201 3h (**Fig. 3I-L**). Amongst the four quadrants, Q2 cells displayed the maximum functional capacity,
202 both in terms of GzmB expression (**Fig. 3I, K**) and bifunctionality, as measured by TNF-$\alpha$ : IFN-$\gamma$
203 double positivity (**Fig. 3J**, **L**). Strikingly, when we selected for CD81+ cells from within the Q2
204 compartment, i.e., a tighter gate for $T^*_{EFF}$ (**Fig. S11E**), this further enriched for effector function,
205 these cells having 2-10x higher expression of both %$GzmB^+$ and % TNF-$\alpha^+$-IFN-$\gamma^+$ compared to
206 other populations (**Fig. 3I-L**). This data supports that sorting for the $T^*_{EFF}$ signature enriches for
207 high-quality effectors.

208 **Prominence of functional effector pool during anti-tumor response:** MC38chOVA tumors
209 are actively controlled in response to the injection of antigen-specific OT-I T cells (**Fig. 4A, Fig.**
210 **S12A**), whereas B78ChOVA are not. We found that *Cd69*-TFP;OT-I T cells in regressing

211 MC38chOVA tumors, retain their predominantly Q2 ($CD69^{+}TFP^{+}$) phenotype even at d12 post
212 adoptive transfer, in contrast to those in the growing B78chOVA tumors(**Fig. 4B-C, Fig. S12B**),
213 while the $TFP^{hi}$ proportions in the corresponding dLNs was similar in both (MC38chOVA :**Fig.**
214 **S12C,** B78chOVA : **Fig. 2C, D**). By two-photon microscopy $TFP^{hi}$ cells could be identified by post-
215 imaging analysis of the appropriate channel intensity over non-TFP controls (**Fig. S12D**). Such
216 analysis showed enhanced cell arrest of the $TFP^{hi}$ within MC38chOVA tumor slices harboring
217 adopted OT-Is, with lower overall motility (**Fig. 4D**), speed (**Fig. S12E**), and persistence of motion
218 (**Fig. S12F)**. In both mouse (*24*) and human(*22*) tumors, these traits are associated with lower T
219 cell exhaustion. Q2 OT-I cells sorted from MC38chOVA tumors also showed the highest killing
220 capacity when exposed to MC38chOVA cells in vitro (**Fig. 4E**). In MC38 as in the B78 model,
221 CD81 was enriched specifically in Q2 cells among intratumoral OT-Is (**Fig. S12G**). Using that
222 surface marking, we found that CD81 was markedly more abundant in the ongoing antigen-
223 specific anti-tumor response in MC38 tumors (**Fig. S12H**), as opposed to non-responsive
224 B78chOVA and PyMTchOVA tumors (**Fig. S11B, D**). Moreover, Q2 and especially CD81+ $T^{*}_{EFF}$s
225 also enriched for a recently-defined, non-canonical and durable CD39+Ly108+ effector population
226 modestly in B78chOVA and robustly in MC38chOVA tumors. (*27*) (**Fig. S12I**).

227

228 **De novo identification of star effectors by CITE-Seq in human patients:** We next sought to
229 independently identify similar CD8 activation states in human tumors (**Fig. S13A),** now using
230 multimodal CITE-Seq on Head and Neck Squamous Cell Carcinoma (HNSC) tumor biopsies post
231 CD45-enrichment (**Fig. 5A**). We focused first on pooled samples with a large number (~5000) of
232 CD8 T cells, where simultaneous readouts of CD69 mRNA and surface protein allowed CD8 T
233 cells to be gated into 4 quadrants (akin to reporter mice), with notable dominance in Q4 and Q2
234 (**Fig. S13A, B**). Again, presumably due to their rarity and the unbiased nature of combined protein-
235 RNA driven weighted nearest neighbor determination, we did not isolate all Q2 cells into a single

236 cluster. In contrast and akin to mouse studies, Q2 highlighted a subset of cells predominantly
237 concentrated within an effector (Eff-1) subset with some also in the Eff-2, Eff-Exh and naive
238 clusters (**Fig. 5B, C, Fig. S13C, D**).

239 DGE analysis of this small subset of Q2 cells within the Eff-1 cluster (<5% of the total CD8s)
240 revealed a signature comprising of genes associated with activation-related transcription (*CD69,*
241 and also upstream *JUN, FOS, ZFP36, KLF6*) where the former were notably those we initially
242 associated as being downregulated following repeated stimulation. The human-derived signature
243 also included chemokines (*CCL3, CCL4,* both high in the $Tex^{KLR.Eff}$ in mice, **Fig. S8A**, *CCL4L2,*
244 *XCL2,* closely related to XCL1 found in the mouse signature), as well as effector function (*IFNG,*
245 *DUSP1,2, NFKBIA, TNFSF9,* etc.), mRNA abundance (*SERTAD1, BTG2*) and proliferation (**Fig.**
246 **5D**). In addition to these genes, the analysis also defined surface protein markers differentially
247 upregulated in these $T^*_{EFF}$s including CCR5 and KLRG1 (**Fig. 5D, Fig. S13E**). Interestingly, the
248 downregulated protein set not only included exhaustion markers CD38, CD39, 2B4, but also
249 CD103 and CD69. Indeed, $T_{RM}$s as defined simply by $CD69^+CD103^+$ exist both in Q2 and Q4 and
250 their relation to exhaustion markers may be context-dependent(*6*) (**Fig. S13E**). Consistent with
251 evolutionary divergence of immune systems(*28*), we found that RNA signatures were not identical
252 and yet across 10 indications of human cancer (*29*), T cell-specific expression of the human $T^*_{EFF}$
253 RNA gene signature correlated highly with that of the expression of human homologs of the RNA
254 signature derived from our mouse tumor scSeq in Fig. 3 (**Fig. 5E)**. Further, when this $T^*_{EFF}$ RNA
255 gene signature was overlaid back onto the UMAP, it again highlighted a region intermediate to
256 and distinct from cells having highest expression of naïve and exhaustion markers (**Fig. 5F**).
257 When applied to other HNSC samples (sample 2 and 3), this RNA $T^*_{EFF}$ signature continued to
258 be highest in cells defined by Q2 and distinct from naïve (variably highest in Q1 and Q3) and
259 exhaustion (predictably highest in Q4) markers alike (**Fig. 5G**). Analysis of CD8 T cells in a
260 second and independent pan-cancer T cell atlas(*30*) again revealed localization of $T^*_{EFF}$ RNA-

261 signature$^{hi}$ cells in the intervening phenotypic space between naïve and exhausted cells (**Fig. 5H,**
262 **Fig. S14A**). Notably, in this second and larger dataset, the authors had suggested multiple T cell
263 subsets associated with enhanced function such as KLR-expressing NK-like CD8 T cells,
264 ZNF683+CXCR6+ $T_{RM}$ (*31*) and IL7R+ memory T cells (*32*) and these were enriched for $T^*_{EFF}$
265 RNA-signature, while exhausted and naïve subsets were not (**Fig. S14B**). Such pan-cancer
266 delineation of potent effectors would likely be refined with generation of more datasets with dual
267 protein and RNA expression to define these populations in distinct settings.

268

269 In summary, we have defined a multimodal approach to find potently activated CD8 T cells, hidden
270 within the largely exhausted pool in tumors. The systematic use of *Cd69* transcription, along with
271 its surface protein expression may be imminently applicable in other important contexts including
272 vaccination, resident memory formation and autoimmunity, to directly identify and study potent
273 activation states of lymphocytes in situ.

274 Here we applied this strategy to isolate and validate that this subpopulation of effector CD8 T cells
275 was functionally superior and otherwise not well illuminated by unbiased RNA-based cell
276 clustering within the well-defined exhaustion paradigm. As future studies seek to better
277 understand and manipulate the $T^*_{EFF}$ cells, it is interesting to speculate that chemokines like
278 XCL1/XCL2 would allow $T^*_{EFF}$s to attract the superior antigen presenting XCR1+ DCs to interact
279 and drive a reactive archetype. These cells may indeed be generated by potent stimulation driven
280 by cDC1s (*33*). While exploration of favorable cDC1 niches and networks continue to drive the
281 field, the identification of functional $T^*_{EFF}$s now opens up the possibility to focus on directly
282 detecting, studying and ultimately enhancing potent effectors in tumors, as an optimizing strategy
283 to drive better patient outcomes.

284

## References and Notes:


1. M. L. Broz *et al.*, Dissecting the Tumor Myeloid Compartment Reveals Rare Activating Antigen-Presenting Cells Critical for T Cell Immunity. *Cancer Cell* **26**, 938 (2014).
2. D. Masopust, S. J. Ha, V. Vezys, R. Ahmed, Stimulation history dictates memory CD8 T cell phenotype: implications for prime-boost vaccination. *J Immunol* **177**, 831-839 (2006).
3. B. B. Au-Yeung *et al.*, A sharp T-cell antigen receptor signaling threshold for T-cell proliferation. *Proc Natl Acad Sci U S A* **111**, E3679-3688 (2014).
4. J. N. Mandl, J. P. Monteiro, N. Vrisekoop, R. N. Germain, T cell-positive selection uses self-ligand binding strength to optimize repertoire recognition of foreign antigens. *Immunity* **38**, 263-274 (2013).
5. A. Schietinger *et al.*, Tumor-Specific T Cell Dysfunction Is a Dynamic Antigen-Driven Differentiation Program Initiated Early during Tumorigenesis. *Immunity* **45**, 389-401 (2016).
6. M. JJ *et al.*, Heterogenous Populations of Tissue-Resident CD8+ T Cells Are Generated in Response to Infection and Malignancy. *Immunity* **52**, (2020).
7. J. C. Beltra *et al.*, Developmental Relationships of Four Exhausted CD8+ T Cell Subsets Reveals Underlying Transcriptional and Epigenetic Landscape Control Mechanisms. *Immunity* **52**, 825-841.e828 (2020).
8. B. Daniel *et al.*, Divergent clonal differentiation trajectories of T cell exhaustion. (2021).
9. E. J. Wherry *et al.*, Molecular signature of CD8+ T cell exhaustion during chronic viral infection. *Immunity* **27**, 670-684 (2007).
10. O. Khan *et al.*, TOX transcriptionally and epigenetically programs CD8 + T cell exhaustion. *Nature* **571**, 211-218 (2019).
11. M. Philip *et al.*, Chromatin states define tumour-specific T cell dysfunction and reprogramming. *Nature* **545**, 452-456 (2017).
12. Z. Chen *et al.*, TCF-1-Centered Transcriptional Network Drives an Effector versus Exhausted CD8 T Cell-Fate Decision. *Immunity* **51**, 840-855.e845 (2019).
13. A. C. Scott *et al.*, TOX is a critical regulator of tumour-specific T cell differentiation. *Nature* **571**, 270-274 (2019).
14. K. Kersten *et al.*, Spatiotemporal co-dependency between macrophages and exhausted CD8+ T cells in cancer. *Cancer Cell* **40**, 624-638.e629 (2022).
15. B. L. Horton *et al.*, Lack of CD8 + T cell effector differentiation during priming mediates checkpoint blockade resistance in non-small cell lung cancer. *Sci Immunol* **6**, eabi8800 (2021).
16. W. DA *et al.*, The Functional Requirement for CD69 in Establishment of Resident Memory CD8+ T Cells Varies with Tissue Location. *Journal of immunology* **203**, (2019).
17. J. F. Ashouri, A. Weiss, Endogenous Nur77 Is a Specific Indicator of Antigen Receptor Signaling in Human T and B Cells. *J Immunol* **198**, 657-668 (2017).
18. A. G. Santis, M. López-Cabrera, F. Sánchez-Madrid, N. Proudfoot, Expression of the early lymphocyte activation antigen CD69, a C-type lectin, is regulated by mRNA degradation associated with AU-rich sequence motifs. *Eur J Immunol* **25**, 2142-2146 (1995).
19. T. M. McCaughtry, M. S. Wilken, K. A. Hogquist, Thymic emigration revisited. *J Exp Med* **204**, 2513-2520 (2007).

328 20. N. E. Scharping *et al.*, Mitochondrial stress induced by continuous stimulation under
329 hypoxia rapidly drives T cell exhaustion. *Nature Immunology* **22**, 205-215 (2021).
330 21. J. J. Engelhardt *et al.*, Marginating dendritic cells of the tumor microenvironment cross-
331 present tumor antigens and stably engage tumor-specific T cells. *Cancer Cell* **21**, 402-417
332 (2012).
333 22. R. You *et al.*, Active surveillance characterizes human intratumoral T cell exhaustion. *J Clin*
334 *Invest* **131**, (2021).
335 23. H. Li *et al.*, Dysfunctional CD8 T Cells Form a Proliferative, Dynamically Regulated
336 Compartment within Human Melanoma. *Cell* **176**, 775-789 e718 (2019).
337 24. B. Boldajipour, A. Nelson, M. F. Krummel, Tumor-infiltrating lymphocytes are dynamically
338 desensitized to antigen but are maintained by homeostatic cytokine. *JCI insight* **1**, e89289
339 (2016).
340 25. Y. Sagi, A. Landrigan, R. Levy, S. Levy, Complementary costimulation of human T-cell
341 subpopulations by cluster of differentiation 28 (CD28) and CD81. *Proc Natl Acad Sci U S A*
342 **109**, 1613-1618 (2012).
343 26. K. J. Susa, T. C. Seegar, S. C. Blacklow, A. C. Kruse, A dynamic interaction between CD19
344 and the tetraspanin CD81 controls B cell co-receptor trafficking. *Elife* **9**, (2020).
345 27. J.-C. Beltra *et al.*, Enhanced STAT5a activation rewires exhausted CD8 T cells during
346 chronic stimulation to acquire a hybrid durable effector like state. (2022).
347 28. T. Shay *et al.*, Conservation and divergence in the transcriptional programs of the human
348 and mouse immune systems. *Proc Natl Acad Sci U S A* **110**, 2946-2951 (2013).
349 29. A. J. Combes *et al.*, Discovering dominant tumor immune archetypes in a pan-cancer
350 census. *Cell* **185**, 184-203.e119 (2022).
351 30. L. Zheng *et al.*, Pan-cancer single-cell landscape of tumor-infiltrating T cells. *Science* **374**,
352 abe6474 (2021).
353 31. M. Di Pilato *et al.*, CXCR6 positions cytotoxic T cells to receive critical survival signals in
354 the tumor microenvironment. *Cell* **184**, 4512-4530 e4522 (2021).
355 32. G. Micevic *et al.*, IL-7R licenses a population of epigenetically poised memory CD8(+) T
356 cells with superior antitumor efficacy that are critical for melanoma memory. *Proc Natl*
357 *Acad Sci U S A* **120**, e2304319120 (2023).
358 33. J. CS *et al.*, An intra-tumoral niche maintains and differentiates stem-like CD8 T cells.
359 *Nature* **576**, (2019).
360 34. K. C. Barry *et al.*, A natural killer-dendritic cell axis defines checkpoint therapy-responsive
361 tumor microenvironments. *Nat Med* **24**, 1178-1191 (2018).
362 35. M. K. Ruhland *et al.*, Visualizing Synaptic Transfer of Tumor Antigens among Dendritic
363 Cells. *Cancer Cell* **37**, 786-799.e785 (2020).
364 36. Y. S. Tan, Y. L. Lei, Isolation of Tumor-Infiltrating Lymphocytes by Ficoll-Paque Density
365 Gradient Centrifugation. *Methods Mol Biol* **1960**, 93-99 (2019).
366 37. C. S. McGinnis *et al.*, MULTI-seq: sample multiplexing for single-cell RNA sequencing using
367 lipid-tagged indices. *Nat Methods* **16**, 619-626 (2019).
368 38. G. Oliveira *et al.*, Phenotype, specificity and avidity of antitumour CD8+ T cells in
369 melanoma. *Nature* **596**, 119-125 (2021).

39. S. J. Carmona, I. Siddiqui, M. Bilous, W. Held, D. Gfeller, Deciphering the transcriptomic landscape of tumor-infiltrating CD8 lymphocytes in B16 melanoma tumors with single-cell RNA-Seq. *Oncoimmunology* **9**, 1737369 (2020).
40. E. Kim *et al.*, Inositol polyphosphate multikinase is a coactivator for serum response factor-dependent induction of immediate early genes. *Proc Natl Acad Sci U S A* **110**, 19938-19943 (2013).
41. A. Litvinchuk *et al.*, Complement C3aR Inactivation Attenuates Tau Pathology and Reverses an Immune Network Deregulated in Tauopathy Models and Alzheimer's Disease. *Neuron* **100**, 1337-1353.e1335 (2018).
42. A. S. Stephens, S. R. Stephens, N. A. Morrison, Internal control genes for quantitative RT-PCR expression analysis in mouse osteoblasts, osteoclasts and macrophages. *BMC Res Notes* **4**, 410 (2011).
43. A. Dobin *et al.*, STAR: ultrafast universal RNA-seq aligner. *Bioinformatics* **29**, 15-21 (2013).
44. B. Li, C. N. Dewey, RSEM: accurate transcript quantification from RNA-Seq data with or without a reference genome. *BMC Bioinformatics* **12**, 323 (2011).
45. H. G. Othmer, S. R. Dunbar, W. Alt, Models of dispersal in biological systems. *J Math Biol* **26**, 263-298 (1988).
46. R. B. Dickinson, R. T. Tranquillo, Optimal estimation of cell movement indices from the statistical analysis of cell tracking data. AIChE Journal Volume 39, Issue 12. *AIChE Journal*. 1993.

## Acknowledgments:

***Funding:***

National Institutes of Health Grants: NIH R01CA197363 and NIH R37AI052116

AR was supported by a Cancer Research Institute Postdoctoral Fellowship (CRI2940)

KHH was supported by an American Cancer Society and Jean Perkins Foundation Postdoctoral Fellowship

GH was supported by the National Science Foundation Graduate Research Fellowship Program (NSF2034836)

IZL was supported by Emerson Collective Health Research Scholars Program

We thank Dr. Emily Flynn, UCSF for guidance with the CITE-Seq analysis. We thank Dr. Kelly Kersten, UCSF, Dr. Mike Kuhns, University of Arizona and Dr. Miguel Reina-Campos, University of California San Diego, for critical reading of the manuscript. We also thank Dr. Reina-Campos

for sharing data from Zheng et.al in an analysis-ready format. We thank members of the Krummel lab for their inputs to the manuscript.

***Author Contributions:***

Conceptualization: AR, MFK

Experimentation: AR, MB, GH, LFP, IZL

Mouse scSeq: KHH, AR

Human tumor data analysis: AR, AJC, BS

Human tumor data collection: VD, BD, AJC

Funding acquisition: MFK, AR, KHH

Writing: AR, MFK

Supervision: MFK

***Competing Interests:***

The authors declare no competing interests

***Data materials availability:***

Relevant data will be made publicly available before publication in its final form. Meanwhile, data will be available upon reasonable request, please contact the authors directly.

**List of Supplementary Materials:**

Materials and Methods

Fig. S1-S14

## Figures and Figure Legends:

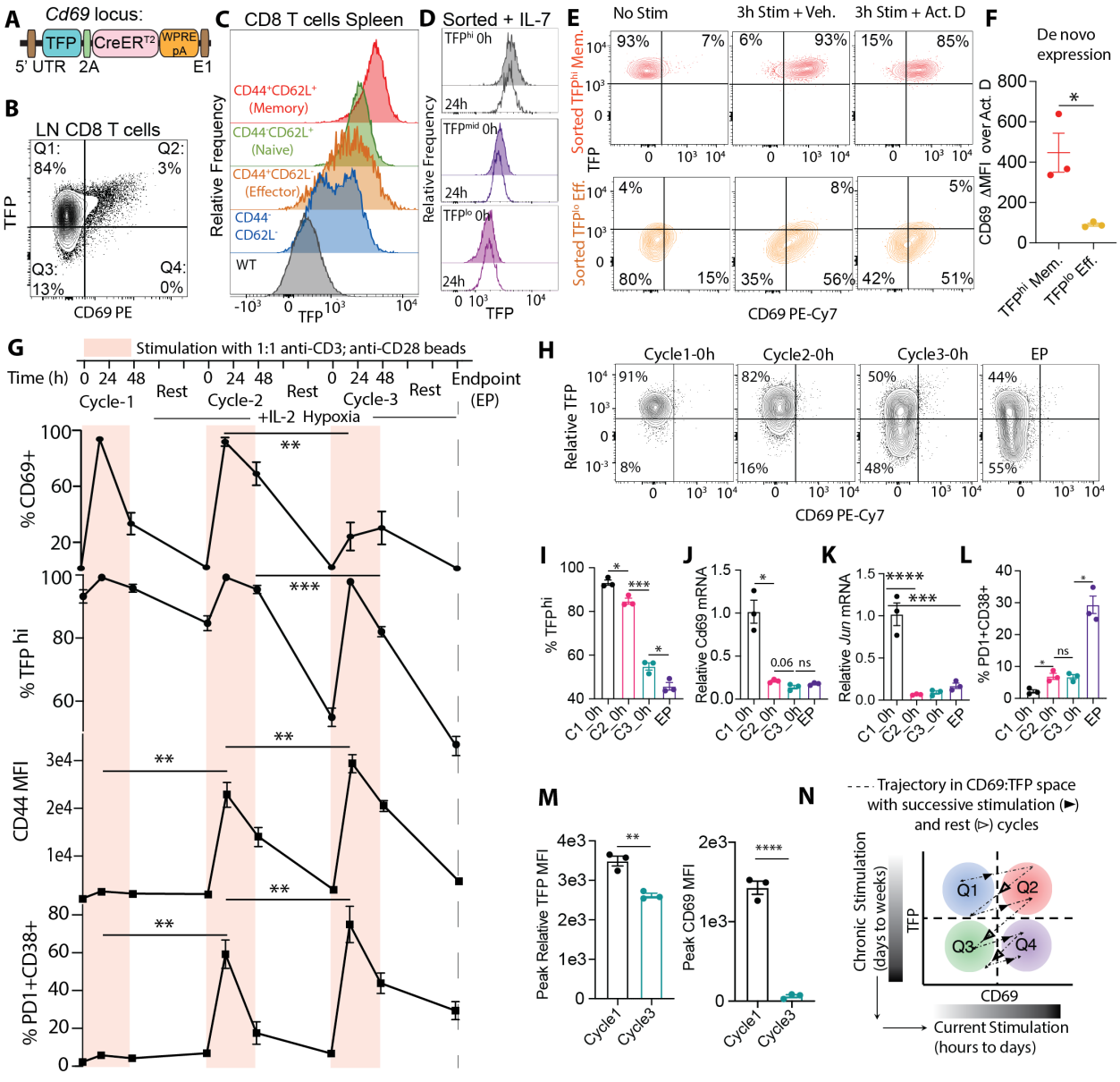


**Fig.1: Cd69-TFP reporter reads out history of T cell stimulation**

**(A)** Design of the TFP-2A-CreER$^{T2}$-WPRE-pA reporter knocked into the 5' UTR of the *Cd69* locus; **(B)** TFP vs. CD69 in homeostatic lymph node (LN) CD8 T cells with percentage of cells in each quadrant; **(C)** representative histograms of TFP expression in splenic CD8 T cells of different phenotypes (as indicated in the figure panel) from an unchallenged Cd69-TFP reporter mouse; **(D)** characteristic histograms of TFP expression from flow cytometry data from sorted TFP$^{hi}$ (top 20%), TFP$^{mid}$ (middle 30%) and TFP$^{lo}$ (bottom 20%) of splenic and lymph node-derived CD8 T cells at 0h and 24h post sort, resting in IL-7; **(E)** flow cytometry

plots of TFP vs. CD69 in sorted TFP$^{lo}$ Effector and TFP$^{hi}$ Memory homeostatic CD8 T cells without stimulation (No Stim), 3h αCD3+αCD28 stimulation + DMSO (3h Stim + Vehicle) or 5μg/mL Actinomycin D (3h Stim + Act.D) and **(F)** relative change in CD69 MFI between the Vehicle and Act D treated conditions (de novo expression) in the two sorted groups, from data in S4B; **(G)** %CD69+, %TFP$^{hi}$, CD44 MFI, %PD1$^{+}$CD38$^{+}$ of freshly isolated CD8 T cells through successive cycles of 48h stimulation and 72h resting in hypoxia + IL-2; **(H)** representative flow cytometry plots showing TFP vs. CD69, **(I)** %TFP$^{hi}$, **(J)** *Cd69* mRNA and **(K)** *Jun* mRNA by qPCR, **(L)** %PD1$^{+}$CD38$^{+}$ at the beginning of cycles 1, 2, 3 and endpoint (EP); **(M)** Peak Relative TFP and CD69 MFI between Cycle 1 and Cycle 3; **(N)** schematic showing the trajectory of CD8 T cells within the TFP:CD69 states (quadrants) with successive stimulation and rest, providing a reading of historic of stimulation. (Plots show mean +/- SEM; TFP negative gates derived from corresponding WT controls; statistical testing by ANOVA and post-hoc Holm-Šídák test; n=3 biological replicates representative of at least 2 independent experiments).

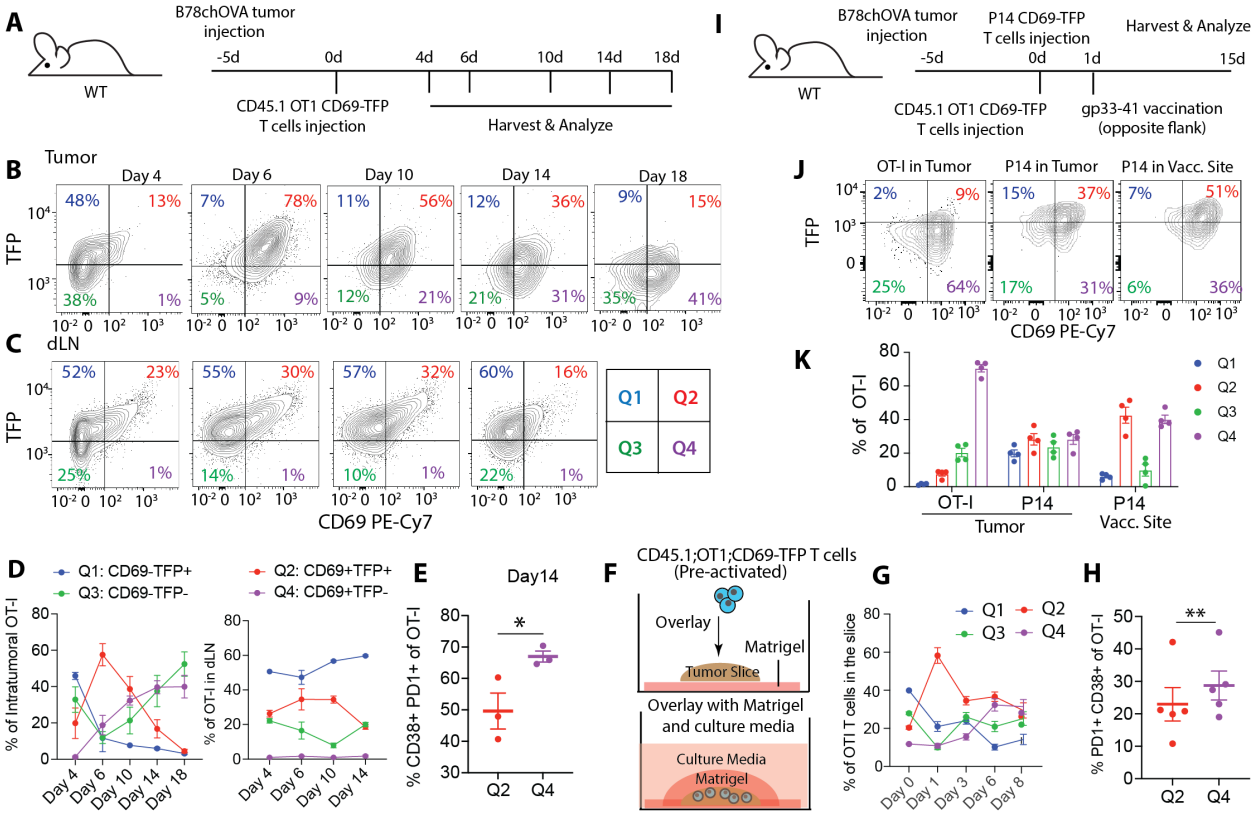

453 **Fig. 2: Delineation of potent versus dysfunctional CD8 T cell activation states in tumors**
454 **(A)** Experimental schematic to track antigen-specific T cells in B78chOVA tumors over time; Flow
455 cytometry plots showing TFP vs. CD69 of adoptively transferred OT-I T cells from **(B)** B78chOVA
456 tumors and **(C)** corresponding tumor-draining lymph nodes (dLN) over time with the **(D)**
457 CD69:TFP quadrant (Q1-Q4) distribution for the same; **(E)** %CD38+PD1+ terminally exhausted
458 cells among activated d14 intratumoral OT-Is belonging to $TFP^{hi}$ Q2 and $TFP^{lo}$ Q4; **(F)** Schematic
459 representation of long-term tumor slice culture setup; pre-activated: 48h stimulation with
460 αCD3+αCD28 followed by 48h rest in IL-2; **(G)** CD69:TFP quadrant distribution and **(H)**
461 $\%PD1^{+}CD38^{+}$ of slice-infiltrating OT-I T cells at d8; **(I)** Experimental schematic of tumor injection
462 and contralateral vaccination with orthogonal antigen specificities; **(J)** Flow cytometry plots
463 showing TFP vs. CD69 profiles of OT-I, P14 T cells in the OVA+ tumor and P14 T cells at the
464 gp33-41 vaccination (vacc.) site; **(K)** CD69:TFP quadrant distribution of the same.
465 (Representative data from 2-3 independent experiments, 3-4 mice or 5-6
466 slices/timepoint/experiment, pre-slice-overlay samples in duplicate, plots show mean +/- SEM, *p
467 <0.05, **p<0.01 by paired t-tests in E and H).
468

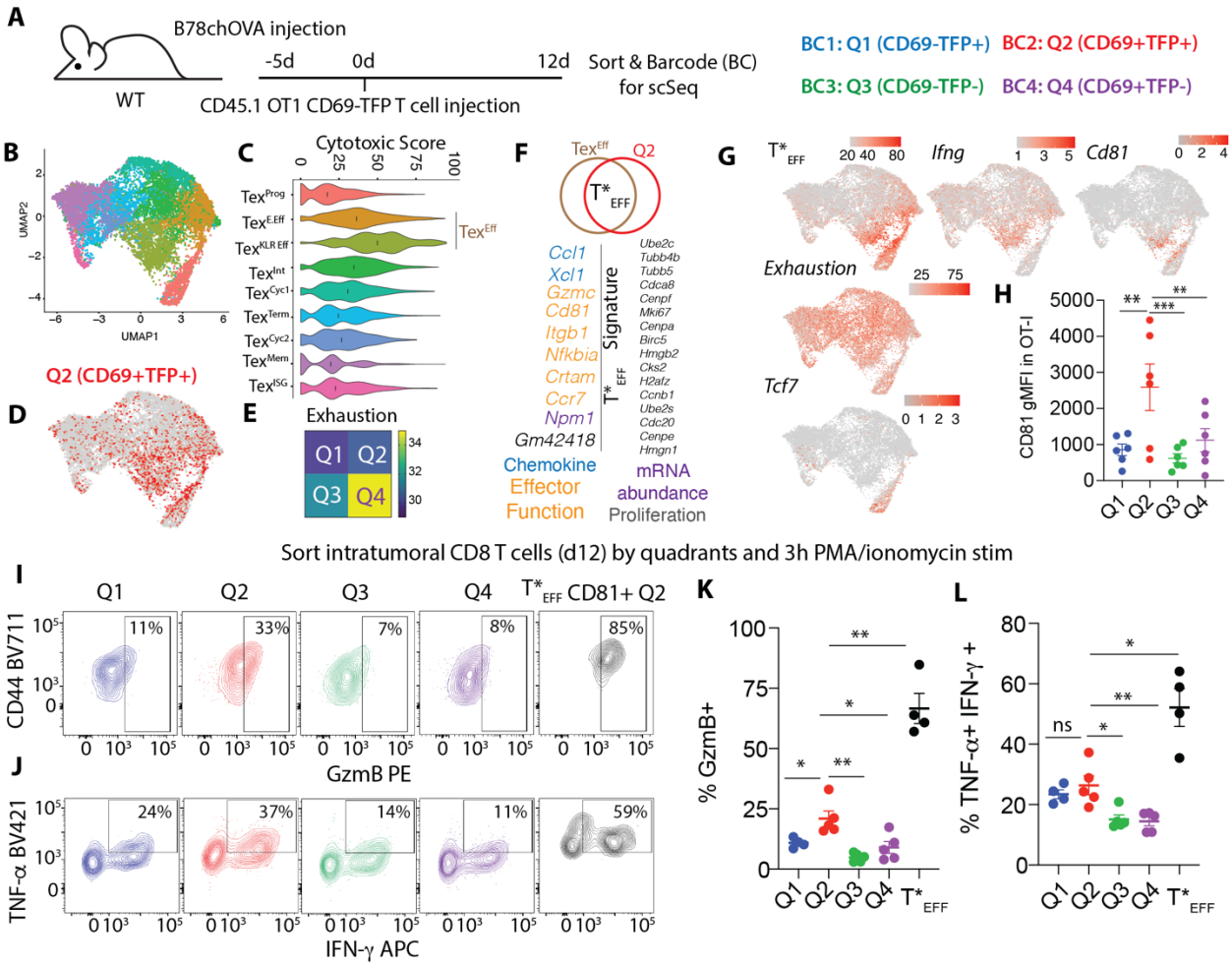


**Fig. 3: Single-cell mapping of activation states reveals functionally endowed intratumoral effectors (A)** Experimental schematic for single cell transcriptomic profiling of intratumoral OT-I T cells sorted by CD69:TFP quadrants; **(B)** UMAP representation of the scSeq data color-coded by computationally-derived clusters; **(C)** Cytotoxic scoring of the T cell subsets (black lines =median); **(D)** overlay of Q2 ($CD69^{+}TFP^{+}$) in the UMAP space; **(E)** Heatmap exhaustion score of combined $T_{EX}^{Eff}$ subsets by quadrants; **(F)** Differentially upregulated genes in in Q2 vs. Q4 within the $T_{EX}^{Eff}$ cells to define $T^{*}_{EFF}$ signature (color-coded text indicates predicted function of similarly colored genes); **(G)** Overlay of $T^{*}_{EFF}$ signature score, *Ifng, Cd81,* Exhaustion Score, and *Tcf7* in the UMAP space; **(H)** CD81 expression in d14 intratumoral OT-I T cells grouped by quadrants; Intracellular expression of **(I)** GzmB, **(J)** TNF-α and IFN-γ in intratumoral OT-I T cells sorted by quadrants and restimulated, with a sub-gating of $CD81^{+}$ cells from Q2, with **(K and L)** corresponding quantification. pooled data from 2 independent experiments with 2-3 biological replicates (sorted cells from 2-3 tumors each)/experiment (K, L). Plots show mean +/- SEM; null hypothesis testing by paired RM ANOVA with post-hoc paired t-tests.

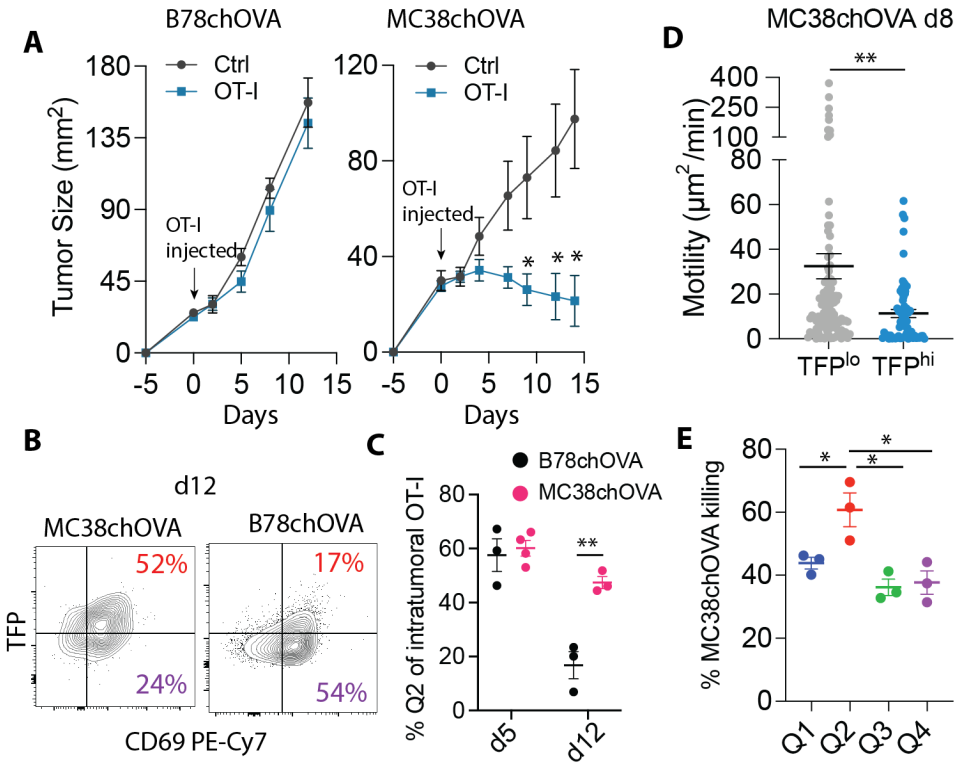


**Fig. 4: Prominence of potent CD8 effectors in favorable anti-tumor response**

**(A)** Contrasting growth curves of B78chOVA and MC38chOVA with and without OT-I transfer 5 days post tumor injection, as indicated by the color-coded arrows (n=5-6/group); **(B)** Typical flow cytometry plot of TFP vs. CD69 of intratumoral OT-Is d12 post adoptive transfer with **(C)** quantification of the percentage of Q2 cells at d5 and d12 in the two tumor models; **(D)** Motility of $TFP^{hi}$ vs. $TFP^{lo}$ intratumoral OT-Is d8 post adoptive transfer within live MC38chOVA tumor slices; **(E)** in vitro killing of MC38chOVA cells by OT-I T cells sorted by CD69:TFP quadrants from d8 MC38chOVA tumors; Bar plots show mean +/- SEM; n > 100 cells per group pooled from at least 2 slices each from different tumors (D); null hypothesis testing by unpaired t test (C), Mann-Whitney U test (D), ANOVA with post-hoc Holm-Šídák test (E).

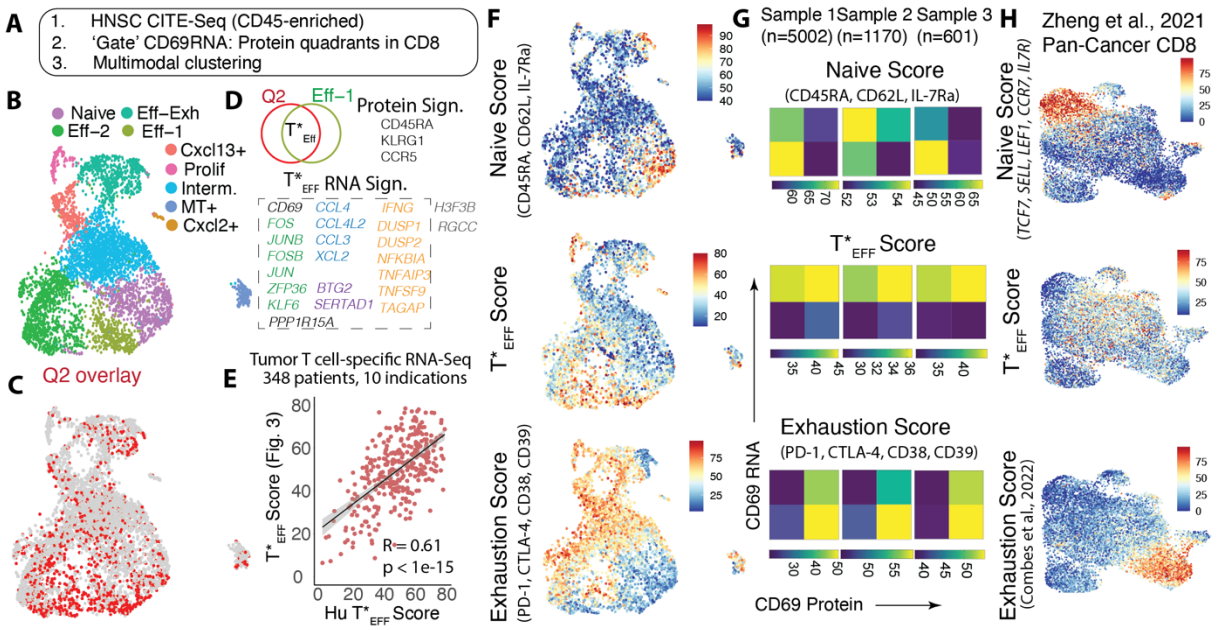


**Fig. 5: De novo identification of potent effectors in human cancer by CITE-Seq**

**(A)** Schematic description of human HNSC tumor CITE-Seq analysis; (B) UMAP showing weighted nearest neighbor (WNN) determined clusters by multimodal RNA and Protein analysis; (C) overlay of Q2 cells (determined by gating on CD69 Protein and RNA – Fig.S13B) on the UMAP; (D) Differentially upregulated genes and proteins in the $T^*_{EFF}$ (Q2 ∩ Eff-1) cells vs. all others CD8 T cells, genes color-coded by functional category, box indicates genes used for the $T^*_{EFF}$ gene signature; **(E)** Correlation between this human $T^*_{EFF}$ gene signature and that from human orthologs of the gene signature in Fig. 3F **(F)** Naïve, $T^*_{EFF}$ and Exhaustion scores overlayed on the WNN UMAP, and **(G)** Heatmap representation of median levels of the same scores in CD8 T cells from 3 different patient samples split into CD69 protein: CD69 mRNA quadrants; (n: # of CD8 T cells in each sample); **(H)** Naïve, $T^*_{EFF}$ and Exhaustion scores overlaid onto the UMAP of combined CD8 T cells from a previously published pan-cancer atlas (*30*).

**Supplementary Materials for**

# Multimodal identification of rare potent effector CD8 T cells in solid tumors

Arja Ray[1,2], Molly Bassette[1,2], Kenneth H. Hu[1,2,#], Lomax F. Pass[1,2], Bushra Samad[2,3], Alexis Combes[1,2,3,5], Vrinda Johri[2,3], Brittany Davidson[2,3], Grace Hernandez[4], Itzia Zaleta-Linares[1,2], Matthew F. Krummel[1,2*]

**Affiliations:**

[1]Department of Pathology, [2]ImmunoX Initiative, [3]UCSF CoLabs, [4]Department of Anatomy, [5]Department of Medicine, University of California, San Francisco, CA 94143, USA. [#] Current Address: Department of Immunology, The University of Texas MD Anderson Cancer Center and James P Allison Institute

***Corresponding Author:**
Matthew F. Krummel, Ph.D.
513 Parnassus Avenue, HSW 512
San Francisco, CA 94143-0511
matthew.krummel@ucsf.edu
Tel: (415) 514-3130
Fax: (415) 514-3165

552 **Materials and Methods**

553 ***Mice:*** All mice were treated in accordance with the regulatory standards of the National Institutes
554 of Health and American Association of Laboratory Animal Care and were approved by the UCSF
555 Institution of Animal Care and Use Committee. Cd69-TFP-CreER$^{T2}$ (denoted as Cd69-TFP) mice
556 in the C57BL6/J background were custom-generated from Biocytogen Inc. and then maintained
557 heterozygous (bred to C57BL6/J wild type mice) at the UCSF Animal Barrier facility under specific
558 pathogen-free conditions. C57BL6/J (wild type; WT), C57BL6/J CD45.1 (B6.SJL-Ptprc$^{a}$
559 Pepc$^{b}$/BoyJ), OT-I (C57BL/6-Tg(TcraTcrb)1100Mjb/J) mice were purchased for use from Jackson
560 Laboratories and maintained in the same facility in the C57BL6/J background. For adoptive
561 transfer experiments, CD45.1$^{het}$; OT-I$^{het}$; Cd69-TFP$^{het}$ (denoted simply as CD45.1; OT1; Cd69-
562 TFP) mice were used. Mice of either sex ranging in age from 6 to 14 weeks were used for
563 experimentation. For experiments using the transgenic PyMTchOVA strain(*21*), mammary tumor-
564 bearing females in the age range of 15 to 24 weeks were used. Adoptive transfer of T cells in
565 these mice were done when mice developed at least 2 palpable tumors (> 25-30mm$^2$).

566 **Mouse tumor digestion and flow cytometry:** Tumors from mice were processed to generate
567 single cell suspensions as described previously(*34*). Briefly, tumors were isolated and
568 mechanically minced on ice using razor blades, followed by enzymatic digestion with 200 µg/mL
569 DNAse (Sigma-Aldrich), 100U/mL Collagenase I (Worthington Biochemical) and 500U/mL
570 Collagenase IV (Worthington Biochemical) for 30 min at 37°C while shaking. Digestion was
571 quenched by adding excess 1X PBS, filtered through a 100µm mesh, spun down and red blood
572 cells were removed by incubating with RBC lysis buffer (155 mM $NH_4Cl$, 12 mM $NaHCO_3$, 0.1 mM
573 EDTA) at room temperature for 10 mins. The lysis was quenched with excess 1X PBS, spun down
574 and resuspended in FACS buffer (2mM EDTA + 1% FCS in 1X PBS) to obtain single cell
575 suspensions. Similarly, tumor draining lymph nodes (dLN) were isolated and mashed over 100µm
576 filters in PBS to generate single cell suspensions.

577 For each sample, 2.5-3 million cells/sample were stained in a total of 50µL of antibody mixture for
578 flow cytometry. Cells were washed with PBS prior to staining with Zombie NIR Fixable live/dead
579 dye (1:500) (Biolegend) for 20 min at 4°C. Cells were washed in FACS buffer followed by surface
580 staining for 30 min at 4°C with directly conjugated antibodies diluted in FACS buffer containing
581 1:100 anti-CD16/32 (Fc block; BioXCell) to block non-specific binding. Antibody dilutions ranged
582 from 1:100-1:400, optimized separately. After surface staining, cells were washed again with
583 FACS buffer. For intracellular staining, cells were fixed for 20 min at 4°C using the IC Fixation
584 Buffer (BD Biosciences) and washed in permeabilization buffer from the FoxP3 Fix/Perm Kit (BD
585 Biosciences). Antibodies against intracellular targets were diluted in permeabilization buffer
586 containing 1:100 Fc Block and cells were incubated for 30 min at 4°C followed by another wash
587 prior to readout on a BD LSRII or Fortessa Cytometer.

588 **Processing and flow cytometry analysis of other mouse organs:** To phenotype T cells under
589 from lymphoid organs homeostasis, spleen and inguinal, mesenteric and brachial lymph nodes
590 were isolated and mashed over 100µm filters washed with 1X PBS to generate single cell
591 suspension of lymphocytes. For splenic suspensions, RBC lysis was performed as described
592 above before staining for flow cytometry.

593 To profile thymocytes, thymus was isolated, cut into small pieces with a razor blade and minced
594 by using gentleMACS dissociator (Miltenyi Biotec) in RPMI. Next, the mixture was spun down and
595 resuspended in the digestion mixture described above and allowed to digest with shaking at 37°C
596 for 20 mins, following which, the remaining tissue was either minced again using the gentleMACS
597 dissociator and/or directly mashed over a 100µm filter in FACS buffer to generate a single cell
598 suspension, ready to be processed for staining and flow cytometry.

599 Skin digestion was done as previously described(*35*). Briefly, mice are shaved and depilated prior
600 to removal of dorsal skin. The skin was then rid of fat, minced with scissors and razor blade in the
601 presence of 1 ml of digest media (2 mg/ml collagenase IV (Roche), 1 mg/ml hyaluronidase

602 (Worthington), 0.1 mg/ml DNase I (Roche) in RPMI-1640 (GIBCO). The minced skin was then
603 moved to a 50 ml conical with 5 ml additional digest solution and incubated at 37°C for 45 min
604 with shaking and intermittent vortexing before being washed and passed through a 70μm strainer
605 prior to staining. TFP high vs. low gates were drawn by using a side-by-side WT control or using
606 endogenous CD8 T cells in the context of adoptive transfer into a tumor-bearing mouse.

607 **Tumor injections and adoptive transfer of CD8 T cells into tumors:** The B78chOVA and
608 MC38chOVA cancer cell lines, as previously described(*14, 34*), were generated by incorporating
609 the same mcherry-OVA construct used to establish the PyMTchOVA spontaneous mouse
610 line(*21*). For tumor injections, the corresponding cells were grown to near confluency (cultured in
611 DMEM with 10% FCS (Benchmark) and 1% PSG (Gibco)) and harvested using 0.05% Trypsin-
612 EDTA (Gibco) and washed 3x with PBS (Gibco). The number of cells to be injected per mouse
613 was resuspended in PBS and mixed in a 1:1 ratio with Growth Factor Reduced Matrigel (Corning)
614 to a final volume of 50μL per injection. The mixture was injected subcutaneously into the flanks
615 of anesthetized and shaved mice. Tumors were allowed to grow for 14–21 days unless otherwise
616 noted, before tumors and tumor-draining lymph nodes were harvested for analysis. CD8 T cells
617 were isolated from CD45.1;OT-1;Cd69-TFP mice using the EasySep Negative Selection Kit (Stem
618 Cell Bio), resuspended in 1X PBS at 10X concentration 100μL was injected into each tumor-
619 bearing mice. For B78chOVA and PyMTchOVA tumors, 1 million and for MC38chOVA tumors,
620 200,000 CD8 T cells were injected retro-orbitally into each mouse either 5d (B78chOVA), 7d
621 (MC38chOVA) post tumor injection or when mice had at least 2 palpable tumors (PyMTchOVA).
622 Tumor measurements were done by measuring the longest dimension (length) and approximately
623 perpendicular dimension (width) using digital calipers, rounded to one decimal place each.

624 **Contralateral tumor injection and vaccination:** 5 days post B78chOVA tumor injection, equal
625 numbers (1 million) CD8 T cells from a CD45.1;OT-I;Cd69TFP and P14;Cd69TFP mice were
626 injected retroorbitally into each mice. Next day, gp33-41 subcutaneous peptide (Anaspec)

627 vaccination was injected contralaterally to the tumor, with 50µg peptide + 50µL Common Freund's
628 Adjuvant (CFA, Sigma) along with 50µL PBS for a total volume of 100µL. The vaccination site
629 was identified by a white, hardened subcutaneous mass and isolated and processed similarly to
630 the tumor for flow cytometry.

631 **In vitro stimulation of naïve CD8 T cells:** CD8 T cells were isolated from Cd69-TFP or WT mice
632 as described above and plated in a 96 well round bottom plate (Corning) at 80,000 cells/well in T
633 cell media-RPMI (Gibco) + 10% FCS (Benchmark) + Penicillin/Streptomycin + Glutamine (Gibco).
634 TCR stimulation was induced by adding anti-CD3/CD28 Dynabeads (Applied Biosystems) at the
635 concentration of 2µL per 80,000 cells (1:1 ratio of cells:beads), the plate was briefly spun down
636 to bring cells and beads together before incubation at 37°C for varying lengths of time. 55µM β-
637 mercaptoethanol (BME; Gibco) was added to the T cell media during stimulation. For repeated
638 stimulation assays, 2 wells of each sample at every time point were pooled for mRNA isolation
639 and qRT-PCR, while 2 other wells were used as duplicates for flow cytometry. After each cycle,
640 beads taken off each well and replated for resting in T cell media containing 10 U/mL of
641 Interleukin-2 (IL-2; Peprotech). To restart each stimulation cycle, cells from each biological
642 replicate were pooled, counted and Dynabeads were added at the appropriate concentration for
643 a 1:1 ratio and redistributed into wells for incubation.

644 **Sorting and qPCR, resting or restimulation of homeostatic CD8 T cells:** To sort sufficient
645 CD8 T cells from homeostatic lymphoid organs, CD8 T cells were first isolated from spleens and
646 inguinal, brachial, mesenteric lymph nodes Cd69-TFP or WT mice using the EasySep Negative
647 selection kit. These cells were then sorted on $TFP^{hi}$ (top 15%), $TFP^{mid}$ (middle 30%) and $TFP^{lo}$
648 (bottom 15%) from each mouse separately and rested in T cell media containing 10 U/mL
649 Interleukin-7 in a 96 well round bottom plate and assayed at 0, 24 and 48h. Likewise, for qPCR
650 analysis of populations high, mid and low for TFP, these populations were sorted into cold T cell
651 media, pelleted and subjected to RNA extraction and qPCR with primers for Cd69 and 18s rRNA

652 as the reference gene. For the sort and restimulation experiment, Memory (CD44+CD62L+) TFP$^{hi}$
653 cells and Effector (CD44+CD62L-) TFP$^{lo}$ cells were sorted and incubated in T cell media + 55μM
654 BME containing 1:1 anti CD3/CD28 Dynabeads in a 96 well round bottom plate with either 5μg/mL
655 Actinomycin D (Sigma) in DMSO or DMSO alone (vehicle) for 3h, before profiling by flow
656 cytometry. De novo CD69 surface expression was measured by the difference of CD69 MFI
657 between the vehicle and Actinomycin D treated groups.

658 **Restimulation and cytokine production of intratumoral CD8 T cells:** OT-I T cells from
659 B78chOVA tumors were sorted on a BD FACSAria Fusion or BD FACSAria2 (BD Biosciences) at
660 d11-d13 post adoptive transfer of CD8 T cells from CD45.1; OT-I; Cd69-TFP mice, as described
661 above. To prepare CD45-enriched fractions(*36*), tumors were digested as described above into
662 single cell suspensions, centrifuged and resuspended in 30mL room temperature (RT) RPMI
663 1640. Then, 10mL Ficoll-Premium 1.084 (Cytiva) was carefully underlaid and the tubes
664 centrifuged at 1025g for 20 mins at RT without braking. The resulting interface-localized cells
665 were pipetted out, diluted in equal volume RPMI and centrifuged at 650g for 5 mins to collect the
666 cells. This constituted a CD45-enriched fraction which was then processed for staining and FACS.
667 The four CD69:TFP quadrants were sorted from each tumor sample (cells from 2-3 tumor samples
668 were pooled for a single biological replicate) into serum-coated microcentrifuge tubes containing
669 cold T cell media. These were subsequently plated in a 96-well V-bottom plate either in T cell
670 media or T cell media containing PMA (50 ng/mL; Sigma-Aldrich), Ionomycin (500ng/mL;
671 Invitrogen) + Brefeldin A (3μg/mL; Sigma-Aldrich) and BME (Gibco) for 3h, before cells were
672 collected for surface and intracellular staining for cytokines and granzyme B.

673 **Long-term ex vivo tumor slice overlay:** Tumor slice overlay cultures were adapted, modified
674 and extended from previous work(*22*). For tumor slice overlay cultures, B78chOVA tumors were
675 injected bilateral subcutaneously into the flank of anesthetized and shaved mice. Tumors were
676 allowed to grow for 11 – 13 days. 96 hours prior to tumor harvest and slicing, CD8 T cells were

677 isolated from CD45.1;OT-1;Cd69-TFP mice, as described above. Isolated CD8 T cells were
678 activated via 1:1 culture with Dynabeads Mouse T-Activator CD3/CD28 (Invitrogen) in T cell
679 media + BME in 96 well U-bottom plates for 48 hours. After activation, T cells were removed from
680 Dynabeads rested in T cell media with supplemented 10 U/mL IL-2 (PeproTech) for 48 hours
681 before use. For gating TFP high vs. low cells, CD8 T cells from CD45.1; OT-I mice were subjected
682 to similar pre-treatment and profiled by flow cytometry side-by-side along with the CD45.1;OT-
683 1;Cd69-TFP CD8 T cells at d0.

684 For slicing, tumors were harvested and stored in cold RPMI until use. Each well of a 24 well plate
685 was pre-filled with cold RPMI and stored on ice. Tumors were embedded in 1.5-2% agarose gel,
686 allowed to solidify, and sliced at a thickness of 350 – 400μm using a Compresstome VF310-0Z
687 Vibrating Microtome (Precisionary). Slices were immediately stored in pre-filled 24 well plate on
688 ice until use.

689 For the slice overlay, each well of a 24 well plate was pre-coated with 30μL of 1 part culture
690 medium:4 parts Matrigel and allowed to solidify at 37˚C. Tumor slices were removed from RPMI
691 and excess agarose was trimmed from slice edges (leaving a thin halo of agarose around slices
692 to use for handling). Slices were spread across solidified Matrigel bed in 24 well plates. Rested T
693 cells were stained with Violet Proliferation Dye 450 (BD Biosciences) diluted 1:1000 in PBS at 10
694 x $10^6$ cells/mL for 15 minutes at 37˚C. Cells were washed 2x with PBS and resuspended in T cell
695 culture medium at 150 – 200 x $10^6$ cells/mL. 5μL cell suspension (0.5 – 1 x $10^6$ cells) was added
696 directly on top of each slice and incubated at 37˚C for 3 hours, with 5μL fresh media added to
697 each slice every 30 minutes to prevent slices from drying out. After incubation, 30μL non-diluted
698 Matrigel was added directly atop each slice and allowed to solidify at 37˚C. 2mL T cell culture
699 medium containing BME was added to each well. 1mL culture medium was removed and replaced
700 with fresh medium every 24 hours throughout the experiment.

701 **Single cell RNA Sequencing and Analysis:** Adoptively transferred CD45.1; OT-I; Cd69-TFP
702 CD8 T cells were sorted from B78chOVA tumors d12 post transfer into four populations based on
703 the CD69:TFP quadrants (Q1: TFP+/CD69-, Q2: TFP+/CD69+, Q3: TFP-/CD69-, and Q4: TFP-
704 /CD69+). Sorted cells were separately labeled with lipid and cholesterol-modified oligonucleotides
705 (LMO's) according to McGinnis et. al(*37*). Following 2 washes with PBS + 0.1% BSA, cells were
706 pooled for encapsulation in one lane of a 10X 3' v3 kit with a target cell number of 18,000.

707 Following construction of the GEX library (according to manufacturer's instructions) and the LMO
708 library(*37*), libraries were pooled at a 10:1 molar ratio for sequencing on the NovaSeq 6000. This
709 resulted in 807M cDNA reads and 163M LMO reads. Transcript and LMO reads were counted
710 using the CellRanger count function against the GRCm38 reference genome to generate feature
711 barcode matrices. These matrices were loaded into Seurat and filtered to remove high
712 mitochondrial % cells (> 15%) and cells with low nGene (< 200 genes). Cells were then
713 demultiplexed using their LMO counts with cells having too few LMO nUMI or ambiguous identity
714 (possible multiplets) filtered out using the demultiplex package(*37*). The resulting object had an
715 average cDNA nUMI per cell of 7662 reads and average nGene per cell of 2115 genes and
716 average LMO nUMI per cell of 1080 reads. The final object underwent scaling and then scoring
717 for cell cycle signatures (S and G2M scores as computed using Seurat's built-in CellCycleScoring
718 function. The object then underwent regression for cell cycle effects (S and G2M score as
719 described in the Seurat vignette) and percent mitochondrial reads before PCA. K-Means
720 clustering and UMAP dimensional reduction was then performed on the first 16 PC's.

721 Established subpopulations of exhausted T cells were marked by expression of canonical genes
722 such as Stem-like or Progenitor ($T_{EX}^{Prog}$; *Tcf7, Ccr7, Jun*) (*8, 12*), Early Effector-like ($T_{EX}^{E.Eff}$;
723 *Hsp90aa1, Hsp90ab1, Npm1*) (*38*), Late Effector or KLR-gene-expressing effector-like ($T_{EX}^{KLR.\ Eff}$;
724 *Klrd1, Zeb2*) (*8*), Memory $T_{EX}^{Mem}$. (*Cxcr3, Ly6c2, Itgb7)* (*39*) and Interferon-Stimulated $T_{EX}^{ISG}$
725 (*Cxcl10, Isg15, Ifit1*) (**Fig. S8A**). The Intermediate ($T_{EX}^{Int.}$) and Terminal ($T_{EX}^{Term.}$) subsets were

726 distinguished by exhaustion-related genes *Ctla4, Pdcd1, Tox* and those related to actin
727 organization and TCR signaling such as *Tmsb4x, Coro1a, Actg1, Ccl5 and S100a6(8).*
728 Additionally, two cell cycle gene-dominated clusters termed $T_{EX}^{Cyc1}$ $T_{EX}^{Cyc2}$ were identified (**Fig.**
729 **3B, Fig. S8A**).

730 Cytotoxic and exhaustion scores were generated by calculating the average expression of
731 ensemble gene lists for each of the phenotypes—Exhaustion: *Ctla4, Pdcd1, Cd38, Entpd1, Tox*;
732 Cytotoxic: *Prf1, Gzmc, Tnfrsf9, Ifng, Klrd1*.

733 **qRT-PCR:** At designated time points, CD8 T cells were isolated from the 96 well culture plates,
734 or CD8 T cells were sorted into T cell media and centrifuged. The supernatant was aspirated out
735 and the pellets stored at -80˚C until mRNA extraction using the RNEasy Micro Kit (Qiagen).
736 Corresponding cDNA was synthesized from the mRNA samples using the cDNA amplification kit
737 (Applied Biosystems). qPCR using pre-designed *Cd69* and *18s* probes (Invitrogen) with a
738 TaqMan-based assay system (BioRad) or custom-made primers (iDT Technologies) for *Jun* (Fwd:
739 5′ ACGACCTTCTACGACGATGC 3′, Rev: 5′ CCAGGTTCAAGGTCATGCTC 3′)(*40*) , *Stat5a*
740 (Fwd: 5' CGCTGGACTCCATGCTTCTC 3', Rev: 5' GACGTGGGCTCCTTACACTGA 3')(*41*) and
741 *18s* (Fwd: 5' CTTAGAGGGACAAGTGGCG 3', Rev: 5' ACGCTGAGCCAGTCAGTGTA 3')(*42*)
742 using the SsoFast assay system (BioRad) was used to quantify transcripts in a BioRad CFX94
743 machine.

744 **Human tumor samples:** All tumor samples were collected with patient consent after surgical
745 resection under a UCSF IRB approved protocol (UCSF IRB# 20-31740), as described
746 previously(*29*). In brief, freshly resected samples transported in ice-cold DPBS or Leibovitz's L-
747 15 medium before digestion and processing to generate a single-cell suspension. The following
748 cancer indications were included in the cohort: Bladder cancer (BLAD), colorectal cancer (CRC),
749 glioblastoma multiforme (GBM), gynecological cancers (GYN), hepatocellular cancers (HEP),
750 head and neck cancer (HNSC), kidney cancer (KID), lung cancer (LUNG), melanoma (MEL),

751 pancreatic ductal adenocarcinoma (PDAC), pancreatic neuroendocrine tumors (PNET), sarcoma
752 (SRC).

753

754 **Transcriptomic analysis of human tumors:** All tumor samples were collected under the UCSF
755 Immunoprofiler project as described(*29*). Briefly, tumor samples were thoroughly minced with
756 surgical scissors and transferred to GentleMACs C Tubes containing 800 U/ml Collagenase IV
757 and 0.1 mg/ml DNase I in L-15/2% FCS per 0.3 g tissue. GentleMACs C Tubes were then installed
758 onto the GentleMACs Octo Dissociator (Miltenyi Biotec) and incubated for 20 min (lymph node)
759 or 35 min (tumor) according to the manufacturer's instructions. Samples were then quenched with
760 15 mL of sort buffer (PBS/2% FCS/2mM EDTA), filtered through 100μm filters and spun down.
761 Red blood cell lysis was performed with 175 mM ammonium chloride, if needed. Freshly digested
762 tumor samples were sorted by FACS into conventional T cell, Treg, Myeloid, tumor and in some
763 cases, stromal compartments and bulk RNA-seq was performed on sorted cell fractions. mRNA
764 was isolated from sorted fractions and libraries were prepared using Illumina Nextera XT DNA
765 Library Prep kit. The libraries were sequenced using 100bp paired end sequencing on HiSeq4000.
766 The sequencing reads we aligned to the Ensembl GRCh38.85 transcriptome build using
767 STAR(*43*) and gene expression was computed using RSEM(*44*). Sequencing quality was
768 evaluated by in-house the EHK score, where each sample was assigned a score of 0 through 10
769 based on the number of EHK genes that were expressed above a precalculated minimum
770 threshold. The threshold was learned from our data by examining the expression distributions of
771 EHK genes and validated using the corresponding distributions in TCGA. A score of 10
772 represented the highest quality data where 10 out of 10 EHK genes are expressed above the
773 minimum threshold. The samples used for survival analysis and other gene expression analyses
774 had an EHK score of greater than 7 to ensure data quality. Ensemble gene signatures scores

775 were calculated by converting the expression of each gene in the signature to a percentile rank
776 among all genes and then determining the mean rank of all the genes in the signature.

777

778 **Reanalysis of published datasets:** Available, curated RNA-Seq data (*5, 7, 14*) on *Cd69* and
779 upstream transcription factor expression was plotted directly without modification. A curated R
780 object derived from Zheng et al.(*30*) generously shared by Dr. Miguel Reina-Campos, UCSD, was
781 used for analysis in Fig. 5. Ensemble gene signatures were scored as mentioned above and
782 plotted onto pre-existing UMAP dimensional reduction and already annotated cell clusters. While
783 exhaustion and $T^*_{EFF}$ genes were obtained from previously published work (*29*) and this study
784 respectively, *TCF7, SELL, LEF1, CCR7, IL7R* genes were used for the Naïve score.

785

786 **In vitro Killing Assay:** MC38chOVA tumors with adoptively transferred Cd69-TFP-OT-I CD8 T
787 cells in WT B6 mice were harvested at d8 post T cell transfer, digested as mentioned above, and
788 sorted by CD69: TFP quadrants into cold T cell media. Sorted cells were centrifuged,
789 resuspended in fresh, warm T cell media with BME and added onto MC38chOVA cells plated
790 ~24h prior in flat-bottom 96 well plates. To each well containing 5000 MC38chOVA plated 24h
791 prior, 5000 sorted T cells were added. As with the sort and restimulation experiments, each such
792 collection of 5000 cells from a particular quadrant was pooled from 2-3 tumors and treated as a
793 single biological replicate. Each experiment involved 7-8 tumors to obtain at least 3 biological
794 replicates. Technical replicates were included and averaged wherever possible, i.e., at least
795 10,000 cells were sorted from a given quadrant and biological replicate. Percentage killing was
796 obtained by measuring the fractional loss of live cells at 36h in no T cell vs. T cell added conditions
797 relative to 0h. Live cell numbers from each condition was accurately measured by lightly detaching

798 cancer cells with trypsin and scoring against CountBright (ThermoFisher) absolute counting
799 beads on a flow cytometer.

800

801 **CITE-Seq analysis of human tumors:** For CITE-Seq, post tumor digestion, cells were incubated
802 with Human TruStain FcX Receptor Blocking Solution to prevent non-specific antibody binding
803 before staining with Zombie Aqua Fixable Viability Dye and anti-human CD45 antibody in
804 PBS/2%FCS/2mM EDTA/0.01% sodium azide and incubated for 25 min on ice in the dark. Live
805 $CD45^+$ and CD45- cells were sorted on a BD FACSAria Fusion. $CD45^+$ and $CD45^-$ cells were
806 pelleted and resuspended at 1x10^3 cells/ml in 0.04%BSA/PBS buffer before mixing in an 8:2
807 CD45+:CD45- ratio and loaded onto the Chromium Controller (10X Genomics) to generate 5′ v1.1
808 gel beads-in-emulsions (GEM). Pooled 8:2 CD45+:CD45- cells were resuspended in
809 Cell Staining Buffer (BioLegend) and stained with a pool of 137 TotalSeq-C antibodies (Table)
810 according to the manufacturer's protocol before loading onto the Chromium Controller (10X
811 Genomics) for GEM generation. The cDNA libraries were generated using all or a subset of
812 Chromium Next GEM Single Cell 5′ Library Kit for gene expression (GEX), Chromium Single Cell
813 V(D)J Enrichment kit (10X Genomics) for T cell receptor (TCR), and Chromium Single Cell 5′
814 Feature Barcode Library kit for antibody derived tag (ADT) according to the manufacturer's
815 instructions. The libraries were subsequently sequenced on a Novaseq S4 sequencer (Illumina)
816 to generate fastqs with the following mean reads per cell: 42,000 (GEX), 34,000 (TCR), and 5,700
817 (ADT). For multimodal clustering and analysis, CLR normalization followed by weighted nearest
818 neighbor (WNN) clustering was performed using the Seurat package in R. Naïve and Exhaustion
819 scores were generated using the percentile rank method as mentioned above, but with protein
820 (ADT) markers- Naïve : CD62L, CD45RA, IL7RA; Exhaustion: PD-1, CTLA-4, CD38, CD39.

821

822 **Live 2-photon imaging of tumor slices and image analysis:** Live imaging of tumor slices was
823 performed on a custom-made 2-photon microscope as previously described(*1*). Briefly, 1 million
824 CD2dsRed; OT-I; Cd69-TFP or control CD2dsRed; OT-I CD8 T cells were retro-orbitally injected
825 into WT mice bearing MC38chOVA tumors injected 5-7d earlier and harvested 7-10d after T cell
826 injection. Slices for imaging were generated as described above for the ex vivo slice culture assay.
827 Slices were placed in a custom-made perfusion chamber and imaged under oxygenated and
828 temperature-controlled perfusion of RPMI 1640, as described previously(*1*). Dual laser excitations
829 at 825nm and 920nm were used to excite the requisite fluorophores. Image analysis was
830 performed on Imaris (BitPlane) with custom-made plugins developed on Matlab (Mathworks) and
831 Fiji. Surfaces were generated on CD8 T cells and in both CD2dsRed; OT-I and CD2dsRed; OT-
832 I; Cd69-TFP bearing slices and the corresponding levels of the former in the 515-545nm range
833 PMT were used to gate on $TFP^{hi}$ vs. $TFP^{lo}$ OT-Is.

834 Cell tracking was performed on Imaris and corresponding cell positions imported to Matlab for
835 further analysis to fit the persistent random walk model (PRWM) to the cell trajectories(*45*) using
836 the method of overlapping intervals (*46*). Briefly, the mean squared displacement (MSD) for a cell
837 for given time interval $t_i$ was obtained from the average of all squared displacements $x_{ik}$ such that
838

839 $$\overline{x_i} = \frac{1}{n_i}\sum_{k=1}^{n_i} x_{ik} \quad (1)$$

840 and

841 $$n_i = N - i + 1 \quad (2)$$

842 where $n_i$ is the number of overlapping time intervals of duration $t_i$ and N the total number of time
843 intervals for the experiment. Mathematically, the persistent random walk model can be written as

844 $$MSD(t) = n_d S^2 P[t - P\left(1 - e^{-\frac{t}{P}}\right)] \quad (3)$$

845 where S is the migration speed and P is the persistence time. The motility coefficient is given as

$$\mu = S^2 P \quad (4)$$

where $n_d$ is the dimensionality of the random walk (in this case $n_d$=3). We fitted the PRWM in 3D to obtain estimates of speed, persistence time and motility of each cell track by non-linear regression.

**Statistical Analysis:** Statistical analysis was done in GraphPad Prism or in R. For testing null hypothesis between two groups, either Student's t tests and or the non-parametric Mann-Whitney U tests were used, depending on the number and distribution of data points. Likewise, for testing null hypotheses among 3 or more groups, ANOVA or non-parametric tests were performed, followed by post-hoc Holm-Sidak's test, correcting for multiple comparisons. Unless otherwise mentioned, data are representative of at least 2 independent experiments.

## Supplementary Figures:

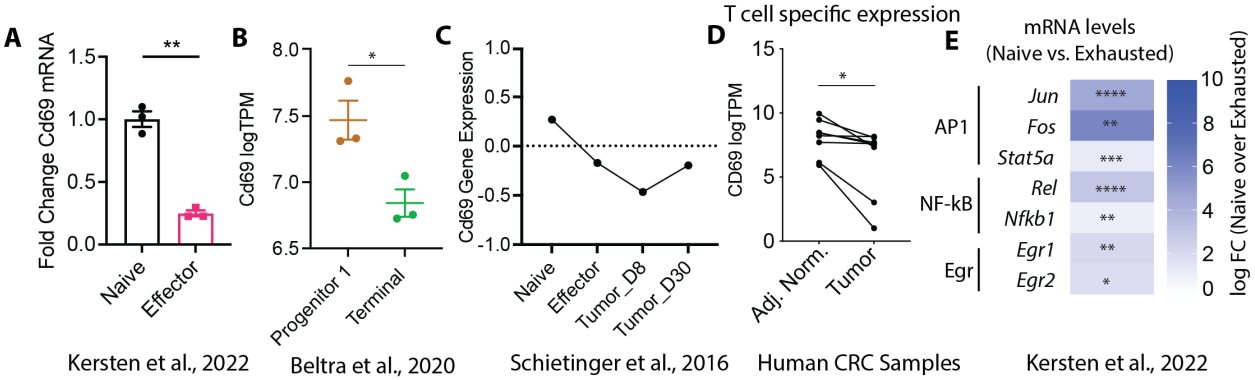


**Fig. S1**: **Resting Cd69 mRNA decreases with T cell differentiation towards exhaustion.** Cd69 mRNA expression in **(A)** Naïve vs. in vitro generated (stimulation with Dynabeads followed by rest in IL-2 containing media) effector CD8 T cells from published RNASeq data(*14*); **(B)** Progenitor 1 and Terminally exhausted T cell subsets from published data (*7*), **(C)** among Naïve, Effector, D8 tumor and D30 tumor infiltrating T cells from other published data (*5*), **(D)** in conventional T cells sorted from tumor and adjacent normal regions of human colorectal cancer patients; **(E)** depressed mRNA expression of factors associated with the Cd69 transcription in Naïve vs. Exhausted CD8 T cells from previous work (*14*) (symbols indicate FDR adjusted p-values). Plots show mean +/- SEM (A, B) p-values obtained by unpaired (A, B) and paired Student's t test (D).

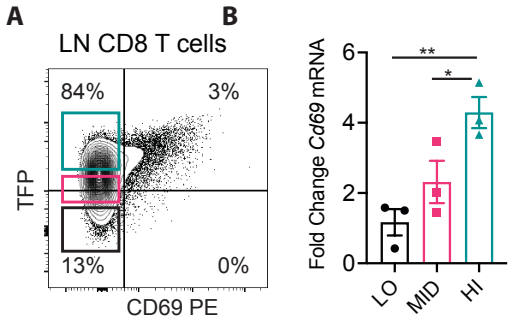


**Fig. S2: Cd69-TFP reporter reads out Cd69 transcription**. **(A)** TFP vs. CD69 in homeostatic lymph node (LN) CD8 T cells with percentage of cells in each quadrant and **(B)** corresponding *Cd69* mRNA by qPCR from color-coded sorted subpopulations.

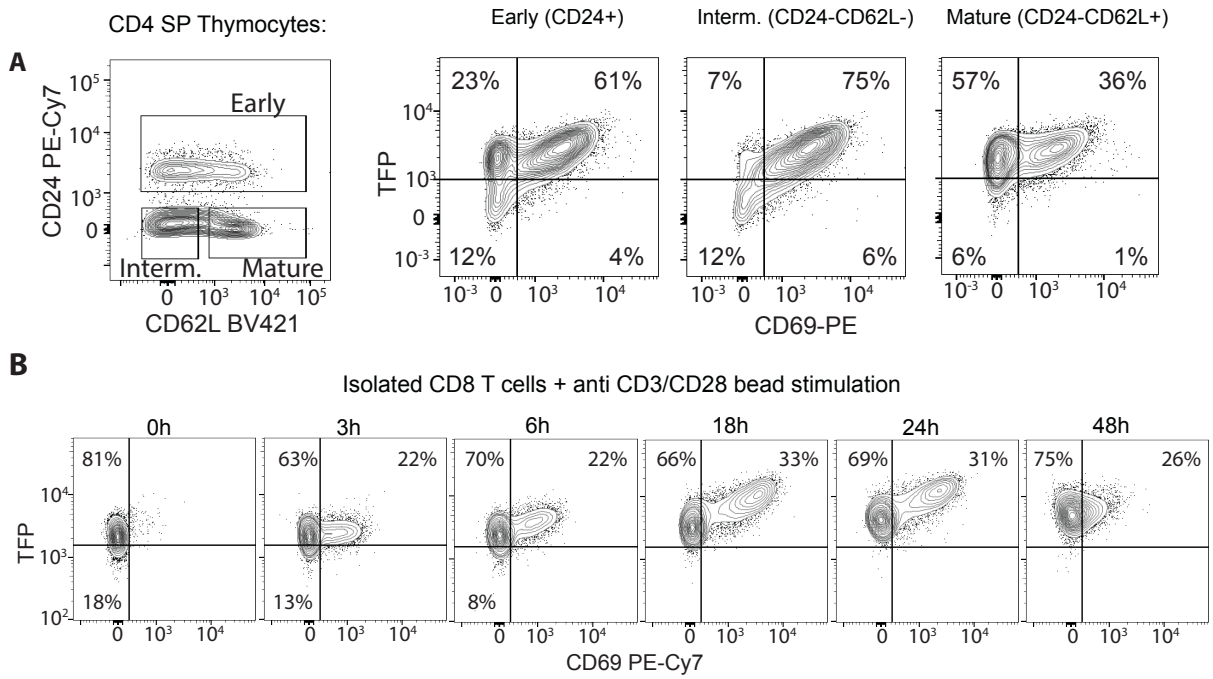


**Fig. S3: TFP is upregulated along with CD69 in known contexts of TCR stimulation. (A)** Representative flow cytometry plot of CD62L and CD24 expression in CD4+CD8- (CD4 single positive or SP) thymocytes to demarcate early, intermediate (interm.) and mature subsets with corresponding plots of TFP vs. CD69 in these subsets with varying degree of maturity during positive selection; **(B)** Representative flow cytometry plots of TFP vs. CD69 of isolated CD8 T cells from a naïve reporter mouse at different time points post stimulation with αCD3+αCD28 Dynabeads;

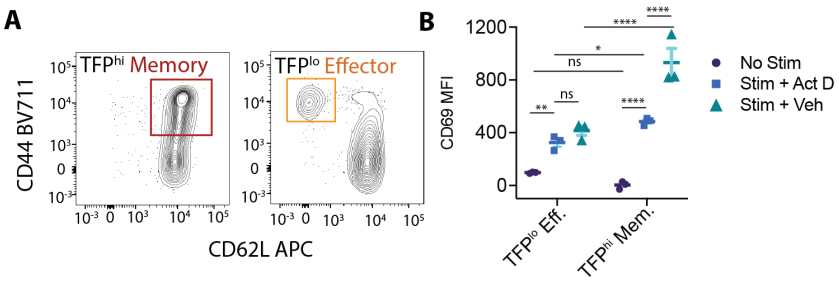


**Fig. S4: Sensitivity to current stimulation is dependent on initial TFP level. (A)** Typical phenotypic profile shown by flow cytometry plots of CD44 vs. CD62L from $TFP^{lo}$ (bottom 20%) and $TFP^{hi}$ (top 20%) splenic CD8 T cells, sorted $TFP^{lo}$ Effector and $TFP^{hi}$ Memory cells are shown by the corresponding color-coded gates matched with Fig. 1E; **(B)** CD69 MFI of the same sorted cells without stimulation (No Stim), 3h αCD3+αCD28 stimulation + DMSO (3h Stim + Vehicle) or 5μg/mL Actinomycin D (3h Stim + Act.D); (data representative of one out of at least 2 independent

experiments, each with 3 mice, bar graphs show mean +/- SEM, null hypothesis testing by unpaired t test, adjusted for multiple comparisons).

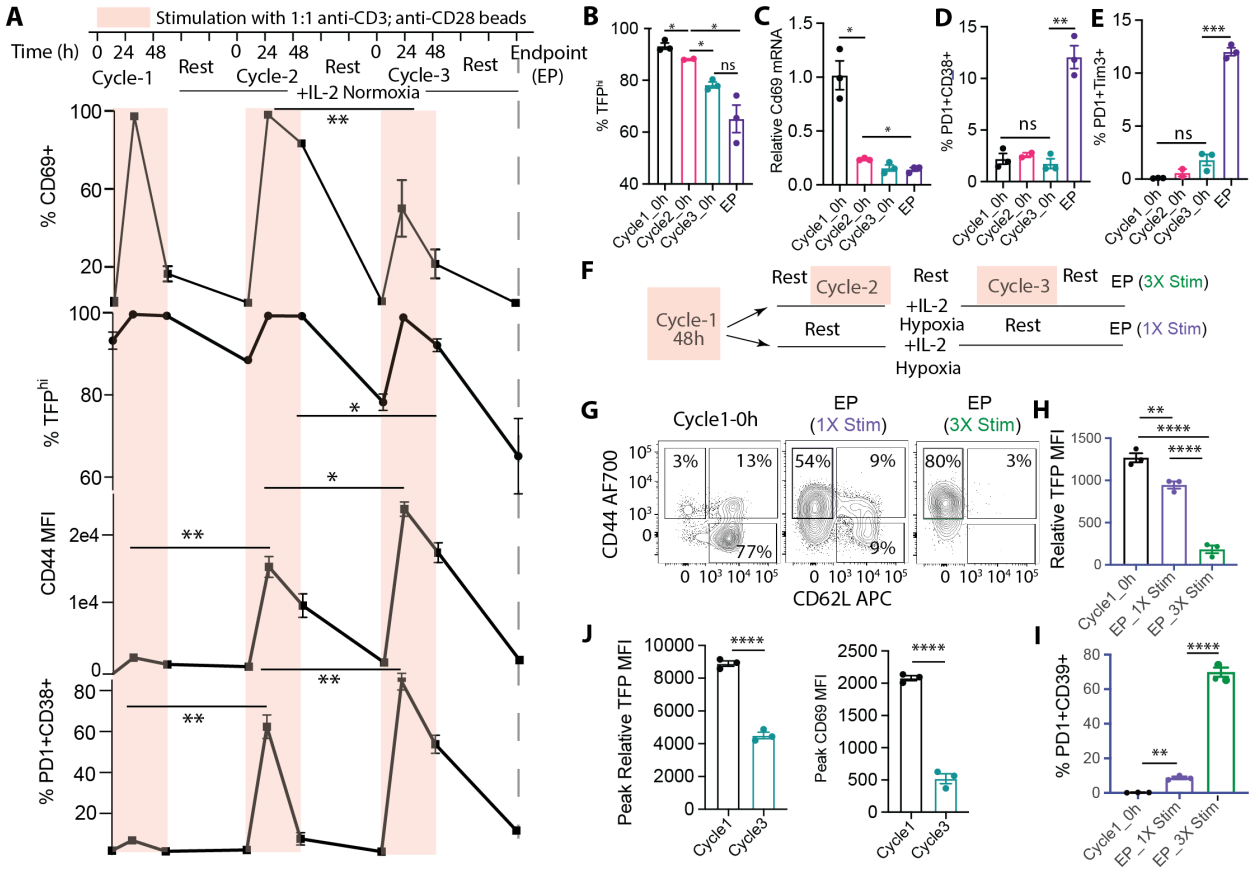


**Fig. S5**: **Repeated TCR stimulation drives down TFP with acquisition of exhaustion markers** **(A)** %CD69+, %TFP$^{hi}$, CD44 MFI, %PD1$^{+}$CD38$^{+}$ of freshly isolated CD8 T cells through successive cycles of 48h stimulation and 72h resting in ambient oxygen (normoxia) + IL-2; **(B)** %TFP$^{hi}$, **(C)** *Cd69* mRNA by qPCR and **(D)** %PD1$^{+}$CD38$^{+}$, **(E)** %PD1$^{+}$Tim-3$^{+}$ at the beginning of cycles 1, 2, 3 and endpoint (EP); **(F)** experimental schematic showing 1X Stim vs. 3X Stim conditions to parse the role of stimulation vs. IL-2 alone; **(G)** flow cytometry plots showing representative CD44 vs. CD62L profiles of CD8 T cells at the timepoints and conditions indicated; for the same experiment, **(H)** TFP (relative to WT control), **(I)** %PD1$^{+}$CD39$^{+}$ of CD8 T cells at the starting point (Cycle1_0h) and at endpoint (EP) either with 1X Stim followed by prolonged rest or 3X stim; **(J)** Peak Relative TFP and CD69 MFI between Cycle 1 and Cycle 3 in normoxia; (bar graphs represent mean +/- SEM; null hypothesis testing by ANOVA followed by post-hoc Holm-Šídák test; data representative of 2 independent experiments, each with 3 mice and technical duplicates/biological replicate at every assay point).

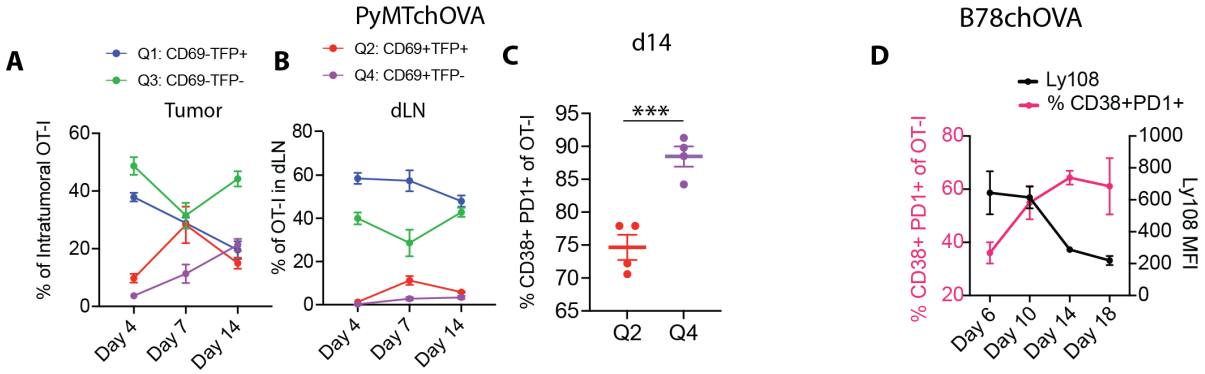


**Fig. S6: Q4, as opposed to Q2 phenotype dominates terminally exhausted OT-Is in tumors** **(A)** TFP:CD69 quadrant distribution of OT-I T cells from a PyMTchOVA tumor or its corresponding **(B)** dLN at different time points post injection into tumor-bearing mice; **(C)** %CD38$^{+}$PD1$^{+}$ terminally exhausted cells among activated d14 intratumoral OT-Is belonging to TFP$^{hi}$ Q2 and TFP$^{lo}$ Q4 from PyMTchOVA tumors; **(D)** %CD38+PD1+ and Ly108 profiles over time (d6-d18) for all intratumoral OT-Is in B78chOVA. Null hypothesis testing by paired t test, bar graphs represent mean +/- SEM; data representative of 2 independent experiments, each with 2-3 mice for PyMTchOVA (each PyMTchOVA mice produced more than one tumor) and >=3 mice for B78chOVA per timepoint.

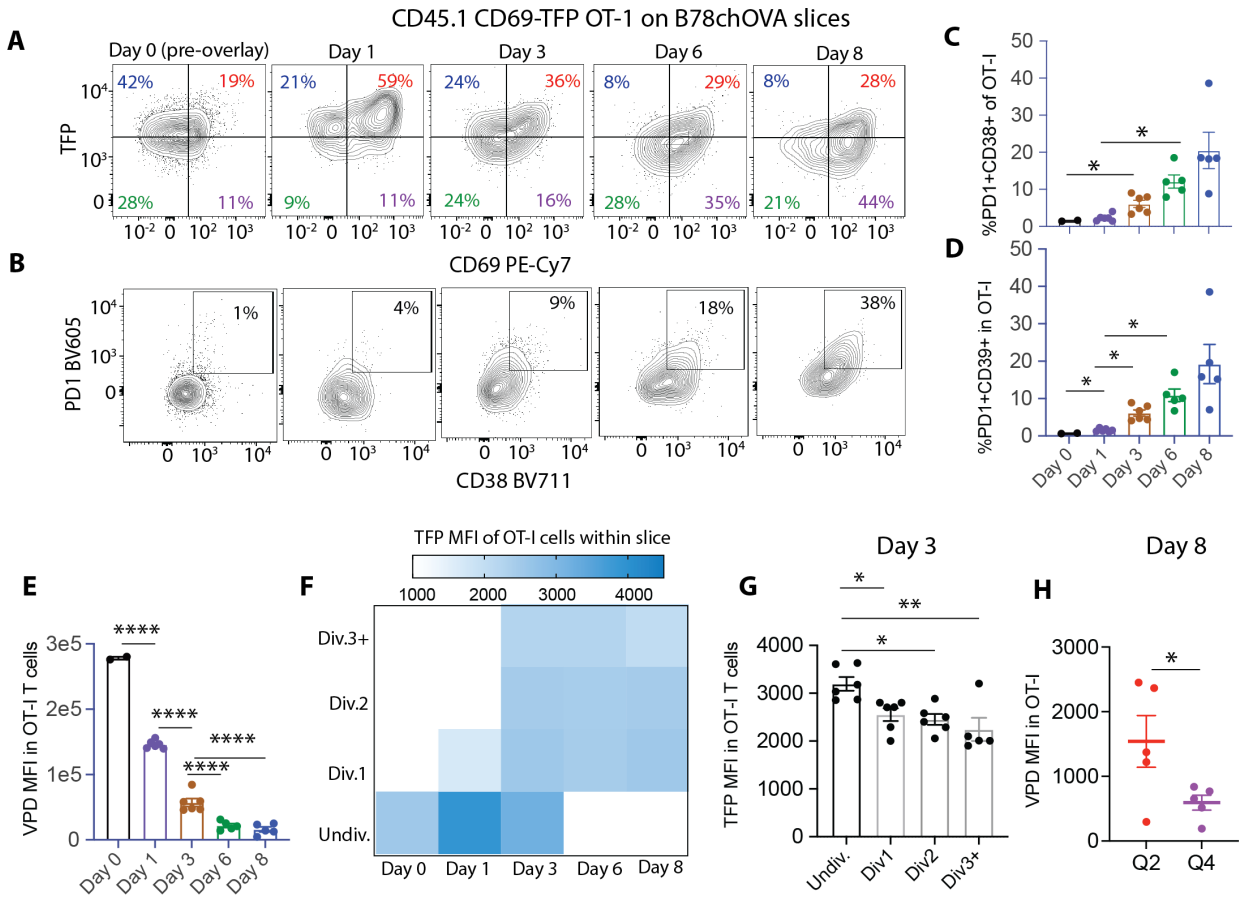


**Fig. S7: Ex vivo tumor slice overlay culture mimics CD69:TFP dynamics in vivo (A)** Representative flow cytometry plots of **(E)** TFP vs. CD69 and **(F)** PD1 vs. CD38 expression in slice-internal OT-I T cell from Day1-Day8, compared to Day0 (pre-overlay); **(B)** %PD1+CD38+, **(C)** %PD1+CD39+ and **(E)** Violet proliferation dye (VPD) MFI of Day 0 pre-overlay and slice-internal OT-I T cells at different time points after slice overlay (Day1-Day8); **(F)** heatmap of average TFP MFI of OT-I CD8 T cells at Day 0 pre-overlay and derived from slice culture from Day 1-Day 8 grouped by estimated number of divisions (>=3, 2, 1, or divided) and **(G)** corresponding bar graph showing this quantification for Day 3; (H) VPD MFI of slice-internal OT-Is from Q2 and Q4 at Day8; Bar graphs and line plots show mean +/- SEM, null hypothesis testing by ANOVA and post hoc Holm-Šídák test, or paired t test in H; data are representative of 2 independent experiments, each 5-6 slices/time point for each slice experiment and Day 0 pre-overlay samples in duplicate; TFP gated on WT controls CD8 T cells.

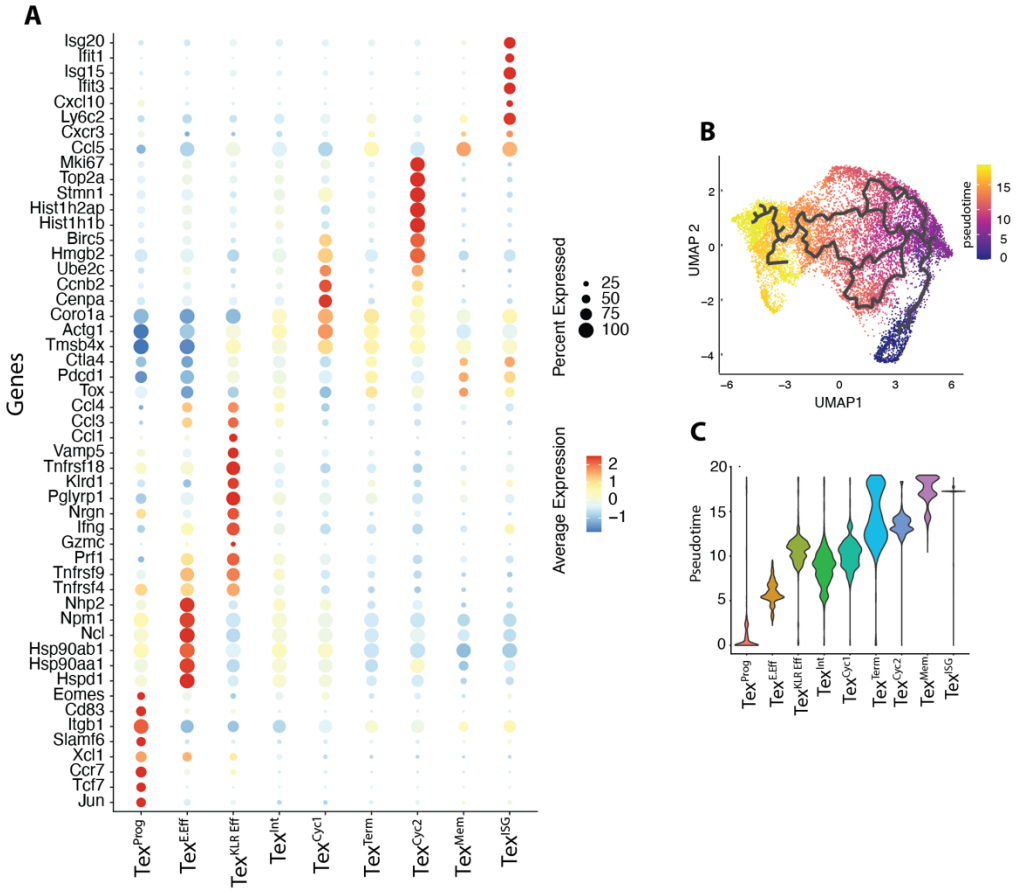


**Fig. S8: Gene expression based clustering of intratumoral OT-Is (A)** Dotplot representation of differentially expressed and canonical $T_{EX}$-associated genes across the computationally derived cell clusters from the scSeq of intratumoral Cd69-TFP:OT-I CD8 T cells at d12 post injection into B78chOVA tumor-bearing mice; **(B)** UMAP representation of the scSeq data color-coded by pseudotime derived from Monocle3 trajectory analysis; **(C)** Pseudotime spread of each cluster.

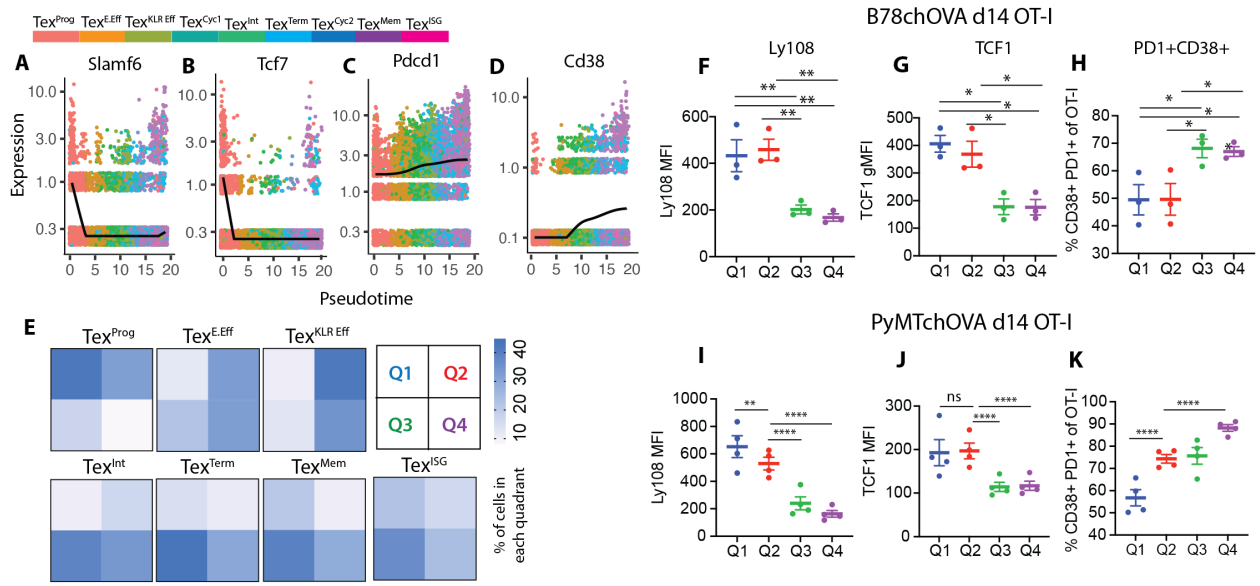


**Fig. S9:Progenitor, intermediate and terminally exhausted CD8 T cells distribute distinctly among CD69:TFP quadrants (A-D)** expression of select genes plotted against pseudotime and color-coded by clusters; best-fitting spline (degrees of freedom=5) to the gene expression pattern overlaid in black, random vertical jitter added to the plot for better visualization; **(E)** heatmaps of percentage of cells by CD69:TFP quadrants Q1-Q4; flow cytometric analysis of select markers from OT-I T cells isolated from **(F-H)** B78chOVA or **(I-K)** PyMTchOVA tumors 14 days post T cell injection grouped by quadrants; (data are mean +/- SEM, representative of >=2 independent experiments with 3-5 mice per experiment, null hypothesis testing by paired RM ANOVA with post-hoc paired t-tests).

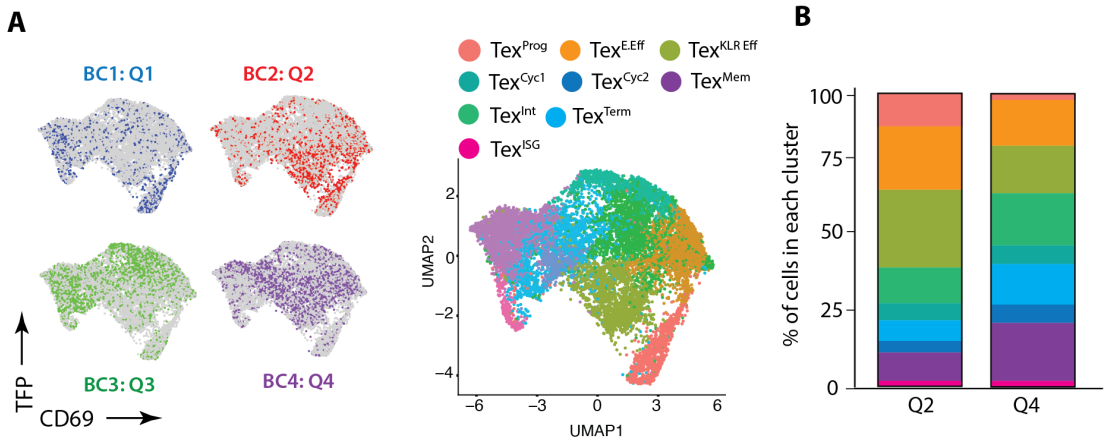

**Fig. S10:Q2 is enriched in effectors but not devoid of terminally differentiated T cells. (A)** Overlay of each CD69:TFP quadrant in the UMAP space with the corresponding clusters shown side-by-side; **(B)** Stacked bar plot showing the distribution of cells in the computationally-defined clusters among all Q2 and Q4 cells.

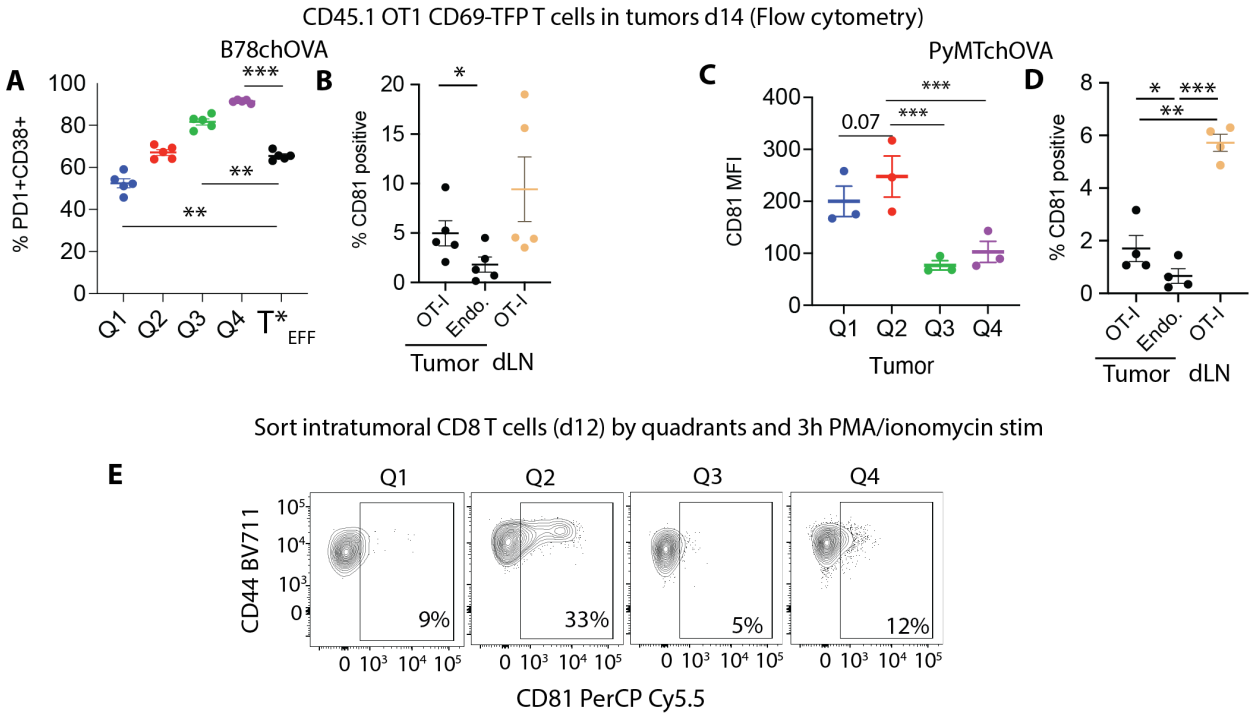


**Fig. S11: CD81 marks a rare subset of cells in Q2 (A)** %PD1+CD38+ of d14 intratumoral OT-I T cells in B78chOVA tumors grouped by quadrants and with a subgating to show CD81+ Q2 ($T^*_{EFF}$) cells; **(B)** % CD81+ among d14 intratumoral OT-I, endogenous T cells and OT-I T cells in the dLN of mice bearing B78chOVA tumors **(C)** CD81 expression in d14 intratumoral OT-I T cells in PyMTchOVA tumors grouped by quadrants and **(D)** % CD81+ among d14 intratumoral OT-I, endogenous T cells and OT-I T cells in the dLN of mice bearing PyMTchOVA tumors (data representative of 2 independent experiments with 3-4 tumors per experiment; **(E)** CD81 expression among the quadrant-sorted populations; Bar graphs show mean +/- SEM; null hypothesis testing by RM ANOVA and post hoc paired t test (A, C) and by ANOVA and post hoc Holm-Šídák test (B, D).

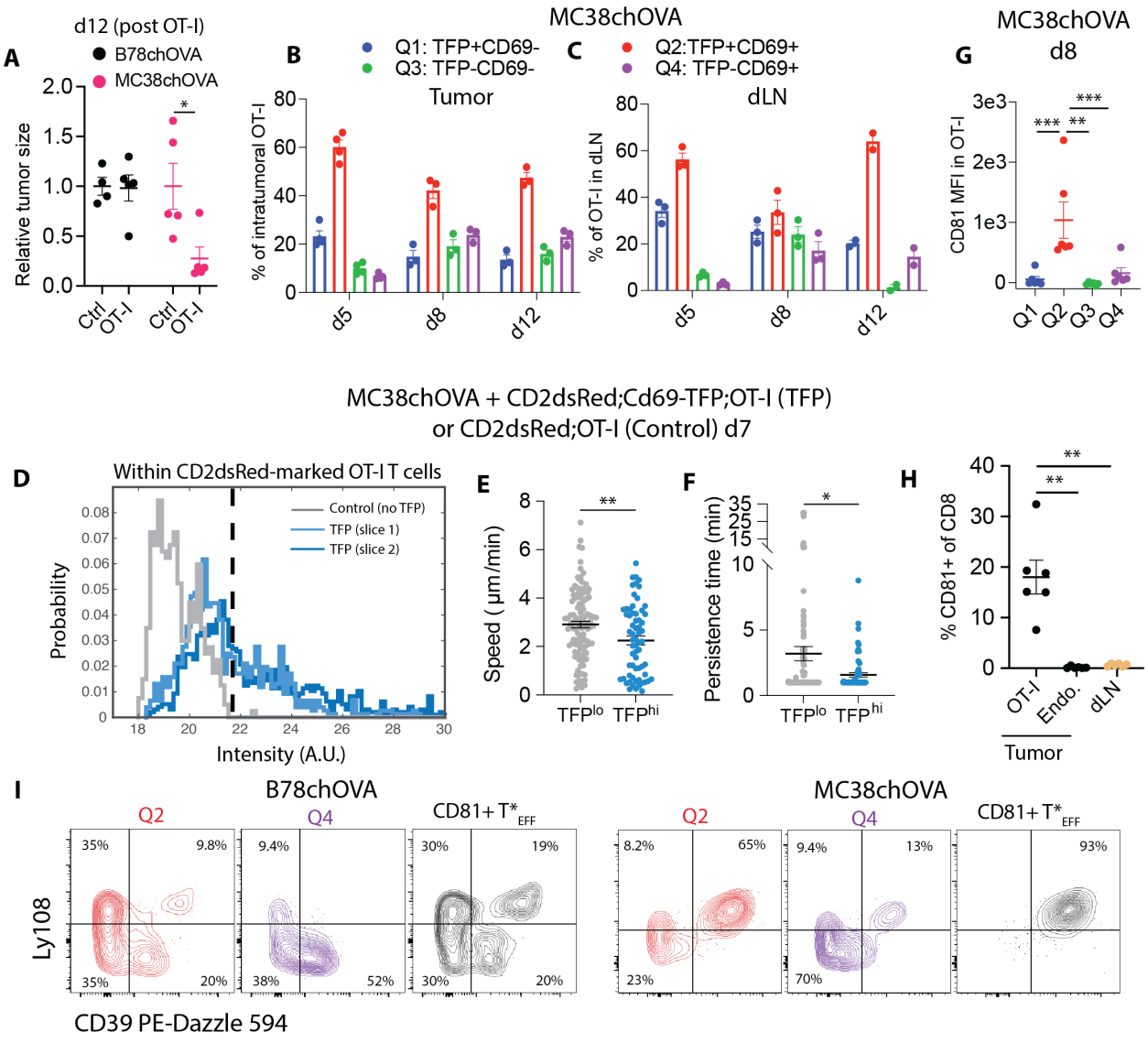


**Fig. S12**: **Features of Q2 OT-I T cells in MC38chOVA tumors. (A)** B78chOVA and MC38chOVA tumor sizes relative to the mean of the Ctrl group d12 post adoptive transfer of Cd69-TFP;CD45.1;OT-I T cells; in Bar graphs showing TFP:CD69 quadrant distribution among OT-I CD8 T cells in **(B)** tumors and **(C)** tdLN at d5, d8, d12 post T cell injection into MC38chOVA tumor-bearing mice corresponding dLNs (n=3-4 mice per group respectively); **(D)** Representative histograms of channel intensity within OT-I T cells in live tumor slices to find $TFP^{hi}$ cells using CD2dsRed and CD2dsRed;Cd69-TFP OT-Is; **(E)** Speed and **(F)** Persistence of $TFP^{hi}$ vs. $TFP^{lo}$ intratumoral OT-Is d8 post adoptive transfer within live MC38chOVA tumor slices; **(G)** CD81 expression in d8 intratumoral OT-I T cells grouped by quadrants; **(H)** % CD81+ among d8 intratumoral OT-I, endogenous T cells and OT-I T cells in the dLN of mice bearing B78chOVA tumors; **(I)** Ly108 vs. CD39 expression profiles in d12 (B78chOVA) and d8 (MC38chOVA)

intratumoral OT-Is, separated by Q2, Q4 and CD81+ T*$_{EFF}$ subsets; bar graphs show mean +/- SEM, null hypothesis testing by unpaired t test (A), Mann-Whitney U test (E, F), paired RM ANOVA with post-hoc paired t-tests.

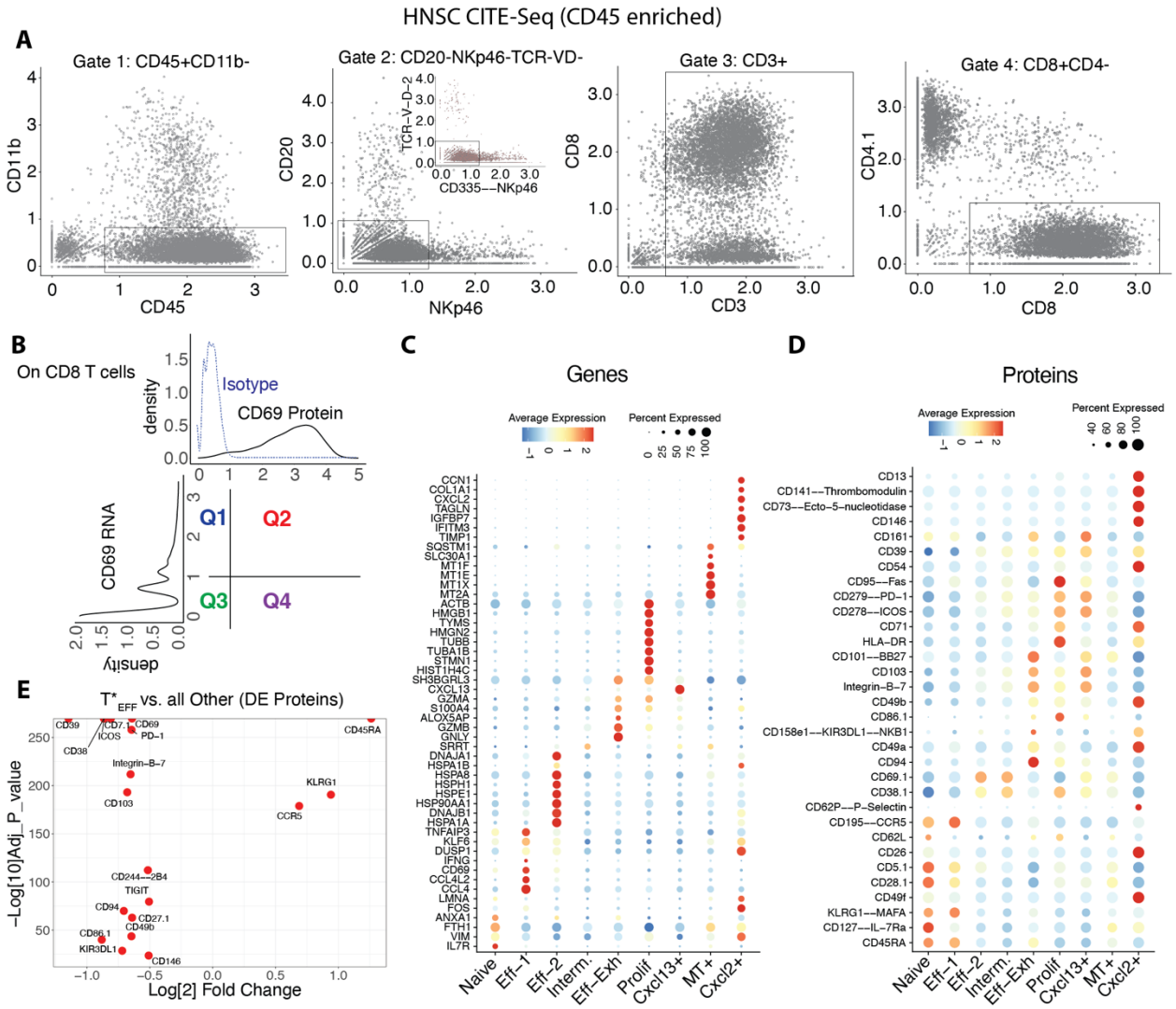


**Fig. S13**: **CITE-Seq of HNSC tumor sample allows mapping of quadrants onto cell phenotypes (A)** Gating scheme of CD45-enriched HNSC CITE-Seq data using protein markers to isolate a pure CD8 population; **(B)** Gating of the CD8 population into CD69 Protein: CD69 RNA quadrants; **(C)** DEGs and **(D)** DE Proteins for the computationally derived subsets obtained through multimodal clustering using both protein and RNA; **(E)** Volcano plot showing DE Proteins in the T*$_{EFF}$ (Q2 $\cap$ Eff-1) vs. all other CD8 T cells pre-filtered by a p-value <0.01 and average abs($\log_2$ fold change) >0.5;

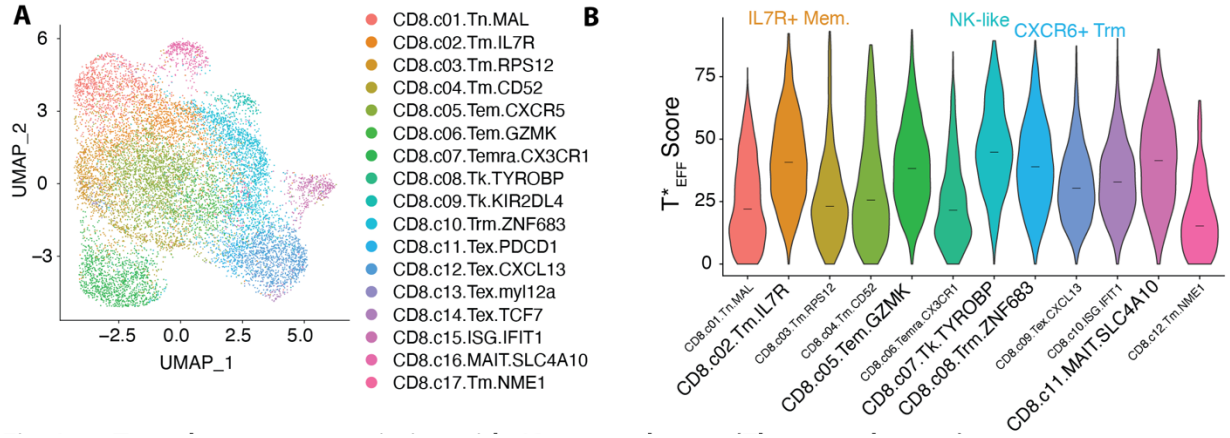


**Fig. S14**: **T*$_{EFF}$ phenotype association with CD8 metaclusters**. **(A)** UMAP representation of computationally-derived subsets among CD8 T cells in a pan-cancer T cell atlas(*30*) and **(B)** Violin plot showing the T*$_{EFF}$ signature score across those subsets – black line denotes median.